



OPEN

Photocatalytic activity of $ZrO_2/TiO_2/Fe_3O_4$ ternary nanocomposite for the degradation of naproxen: characterization and optimization using response surface methodology

Masoud Habibi Zare[✉] & Arjomand Mehrabani-Zeinabad

In this study, ZrO_2 , TiO_2 , and Fe_3O_4 components were synthesized by co-precipitation, sol-gel, and co-precipitation methods, respectively. In addition, solid-state dispersion method was used for synthesizing of $ZrO_2/TiO_2/Fe_3O_4$ ternary nanocomposite. The $ZrO_2/TiO_2/Fe_3O_4$ nanocomposite was characterized by different techniques including XRD, EDX, SEM, BET, FTIR, XPS, EELS, and Photoluminescence (PL). The FTIR analysis of $ZrO_2/TiO_2/Fe_3O_4$ photocatalyst showed strong peaks in the range of 450 to 700 cm^{-1} , which represent stretching vibrations of $Zr-O$, $Ti-O$, and $Fe-O$. The results of FTIR and XRD, XPS analyses and PL spectra confirmed that the solid-state dispersion method produced $ZrO_2/TiO_2/Fe_3O_4$ nanocomposites. The EELS analysis confirmed the pure samples of Fe_3O_4 , TiO_2 and ZrO_2 . The EDAX analysis showed that the $Zr:Ti:Fe$ atomic ratio was $0.42:2.08:1.00$. The specific surface area, pores volume and average pores size of the photocatalyst were obtained $280\text{ m}^2/\text{g}$, $0.92\text{ cm}^3/\text{g}$, and 42 nm respectively. Furthermore, the performance of $ZrO_2/TiO_2/Fe_3O_4$ nanocomposite was evaluated for naproxen removal using the response surface method (RSM). The four parameters such as NPX concentration, time, pH and catalyst concentration was investigated. The point of zero charge of the photocatalyst was 6. The maximum and minimum degradation of naproxen using photocatalyst were 100% (under conditions: NPX concentration = 10 mg/L , time = 90 min , $\text{pH} = 3$ and catalyst concentration = 0.5 g/L) and 66.10% respectively. The stability experiment revealed that the ternary nanocatalyst demonstrates a relatively higher photocatalytic activity after 7 recycles.

Environmental pollution by pharmaceutical compounds is considered as one of the most serious issues in recent years^{1,2}. For the treatment of pharmaceutical wastewater and for removing pollutants before those are released into the environment, identification of the most efficient method is a challenge³. Pharmaceutical wastewater can be treated using physical⁴, chemical, biological⁵, as well as combined methods⁶. The Advanced oxidation processes⁷ including advanced oxidation based on the sulfate radicals⁸, ultraviolet-visible⁹, natural sunlight¹⁰, Fenton oxidation¹¹, electrochemical¹², nanocomposite catalysts¹³, and sonolysis and sono-Fenton¹⁴ have been widely used to remove pollutants from pharmaceutical wastewater with great performance. The formation of radicals during these processes leads to the oxidation of organic pollutants in aqueous solutions. In comparison to other methods, photocatalysis offers several advantages, such as high efficiency, low cost, design of suitable catalysts for specific wastewaters, and high corrosion and temperature stability¹⁵⁻¹⁷. Titanium dioxide (TiO_2) has been widely used as a catalyst in the degradation of organic compounds and pharmaceutical pollutants since it is a light-sensitive semiconductor (including UV and visible light)^{18,19}. The formation of valence band holes and conduction band electrons during photocatalysis produces oxidation-reduction media in wastewater. It can easily degrade organic compounds and convert them into non-toxic compounds such as CO_2 and water^{20,21}. Titanium

Department of Chemical Engineering, Isfahan University of Technology, Isfahan 84156-83111, Iran. ✉email: masoud.habibi@ce.iut.ac.ir

dioxide is a polymorphic material with three crystalline phases: anatase, rutile, and brookite. The anatase phase is more photocatalytically active than the rutile phase^{22,23}. In order to enhance the TiO₂ photocatalyst activity, it is important to use smaller particles (nano size), as smaller particles have higher specific surface areas²⁴. The removal of titanium dioxide nanoparticles after treatment reduces the benefit of this photocatalyst, and immobilization of titanium dioxide (TiO₂) onto supporting materials can be performed, but immobilization reduces the specific surface area in comparison with a homogenous catalysts²⁵. On the other hand, fast recombination of generated electron–hole pairs can decrease the activity of titanium dioxide photocatalyst²⁶. Therefore, some other semiconductors such as ZrO₂ are used to improve of the activity of TiO₂. ZrO₂ doping can slow down the electron–hole pair recombination, strengthen the material and increase surface area and anatase to rutile crystal phases ratio^{27,28}. ZrO₂-TiO₂ photocatalyst has been used to degrade organic compounds, which in this compound, ZrO₂ acts as support or photocatalyst in the system²⁹.

The addition of a small amount of ZrO₂ to TiO₂ can increase the surface area because ZrO₂ inhibits anatase to rutile phase transitions, densification, and crystallite growth by providing dissimilar boundaries³⁰. It was observed that changes in surface chemistry, particularly acidity improve the photocatalyst activity³¹. In this binary catalyst, holes trap such as the hydroxyl groups, prevent electron–hole recombination and oxidation–reduction reactions, and increase quantum yield³¹. In addition to ZrO₂ nanoparticles, it is necessary to be added another compound to these binary metal oxides to improve the surface area of the TiO₂ photocatalyst as well as recovery of TiO₂ from treated wastewater^{32,33}. Magnetic nanoparticles, such as Fe₃O₄, are suitable for this purpose. A Fe₃O₄@TiO₂ photocatalyst has been synthesized to degrade Bisphenol A under visible and long-wavelength UV light irradiation. Moderate iron loading reduced hole-pair separation effectively, and shifted the bandgap in the visible range. Further, the magnetic properties of Fe₃O₄ play a critical role in recovering the used catalyst from the solution, which facilitates practical applications of the Fe₃O₄@TiO₂ photocatalyst³⁴. Fe₃O₄@SiO₂@g-C₃N₄/TiO₂ nanocomposite was used to remove dye pollutants. It has been found that the 10 wt.% g-C₃N₄/TiO₂ composite catalyst can degrade over 91% of anionic and cationic dyes³⁵. Therefore, it is possible to combine the three compounds to degrade toxic and harmful pollutants in wastewater. In recent years, non-steroidal anti-inflammatory drugs (NSAIDs) have been increasingly used for the treatment of COVID-19^{36,37}. Therefore, it is predicted that pharmaceutical-produced wastewater containing NSAIDs such as naproxen will increase and it will be very important to develop an effective method of degradation these compounds from the wastewater. The degradation of naproxen by H₂O₂-modified titanate nanomaterial and Bi-modified titanate nanobulks under visible light irradiation has been successfully accomplished^{38,39}. In previous works, each of these metal oxides was used separately as a catalyst to remove various contaminants^{40–43}, but the interaction of the three metal oxides of Fe₃O₄, TiO₂ and ZrO₂ together and its function to remove pharmaceutical contaminants can produce a synergistic effect. The difference in physical and chemical properties of each component of these nanophotocatalyst makes it unique. A nanocomposite with magnetic, stable, and high photocatalytic properties was finally synthesized^{44,45}. TiO₂ has a band gap of 3.2 eV for anatase, and 3.0 eV for rutile^{46,47}. The ZrO₂ is used as a photocatalyst in heterogeneous reactions due to its semiconductor properties (type n). The band gap energy of ZrO₂ varies from 3.25 to 5.1 eV depending on the sample preparation^{48–55}. Its common band gap energy is 5 eV⁵⁵. It has a wide bandgap and a highly negative flat-band potential, which can be used for hydrogen production through water decomposition^{55,56}. Magnetic properties of Fe₃O₄ nanoparticles make recyclable nanocomposites possible. Furthermore, the excitation range of nanocomposites synthesized from Fe₃O₄ can be used in the visible light range due to their unique optical properties.

The Response surface methodology (RSM) is a widely used mathematical and statistical method for modeling and analyzing a process in which a response is affected by multiple variables, and its goal is to optimize the response^{57,58}. Synthesis of Fe₃O₄/TiO₂/ZrO₂ nanocomposite can improve the photocatalytic property of catalyst. The synthesis of these nanoparticles individually can have some disadvantages such as a wide energy gap, activity only in UV, lower photocatalytic activity, However, their composite synthesis will offer advantages such as higher magnetic properties, recyclable, higher stability and activity, and enhanced photocatalytic activity^{59–67}. The Box–Behnken design (BBD) was used in this study due to its rotatable or nearly rotatable second-order design. The percentage of naproxen degradation was selected as the experimental design response^{68,69}.

The current work is focused on the synthesis of a new ZrO₂/TiO₂/Fe₃O₄ nano-photocatalyst with high photocatalytic activity and reusability for the pharmaceutical wastewater treatment. Its performance has been evaluated in the removal of naproxen from pharmaceutical wastewater under UV light. The synthesised photocatalyst has been characterized with methods such as X-ray diffraction (XRD), Energy Dispersive X-Ray (EDX), Scanning Electron Microscope (SEM), Brunauer–Emmett–Teller (BET), Fourier Transform Infrared Spectroscopy (FTIR), X-ray Photoelectron Spectroscopy (XPS), Electron energy-loss spectroscopy (EELS), and Photoluminescence (PL). We investigated various factors including the initial concentration of naproxen, initial pH of the solution, photocatalyst dosage, and time until the optimal degradation efficiency was obtained using the RSM method.

Experimental and methods

Materials. Titanium (IV) iso-propoxide 97%, zirconyl(IV) chloride octahydrate (ZrOCl₂·8H₂O, 98%), and Iron (II) chloride tetrahydrate (≥99%) and iron (III) chloride hexahydrate(≥99%) were used as a precursors for the synthesis of TiO₂, ZrO₂, and Fe₃O₄ respectively. Ethanol was obtained from Sigma-Aldrich and utilized without any further processing. Deionized water (DI-water) was also used in the experiment. Sulphuric acid (H₂SO₄, 0.1 M) and sodium hydroxide (NaOH, 0.1 M) were used for the adjustment of the pH of the solution. (S)-6 methoxy α -methyl 2-naphthaleneacetic sodium salt was purchased from Sigma Aldrich and its aqueous solution used for degradation experiments. In Table 1, naproxen's physical and chemical properties are shown.

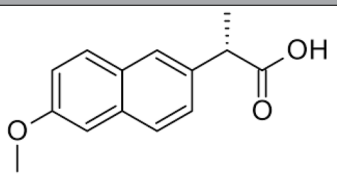
Property	Value
Molecular structure	
Solubility	15.9 mg/L at 25 °C
Melting point	152–154 °C
Log K_{ow}	3.18
p K_a	4.15

Table 1. Physical and chemical properties of naproxen.

Synthesis of nanoparticles. *ZrO₂ nanoparticles.* The co-precipitation method was used for the synthesis of ZrO₂ nanoparticles. Firstly, ZrOCl₂·8H₂O was dissolved in deionized water. Then, 2 M NaOH solution was added to the solution in order to achieve a solution with a pH of 10. The solution was gently stirred for 1 h. After that, the precipitate was filtered, washed with distilled water to reach neutral pH. The obtained powder was dried in an oven at 60 °C for 24 h and then calcined at 700 °C for 10 h⁷⁰.

TiO₂ nanoparticles. Sol–Gel method was used for the preparation of TiO₂ nanoparticles. 15 mL Titanium (IV) isopropoxide was added into 60 mL ethanol. A magnetic stirrer was used to mix the solution for 30 min. 10 mL deionized water in a drop-wise fashion was added into the mixture until hydrolysis reaction occurred in the system. The obtained white gel was dried at 100 °C and later calcined at 450 °C for 2 h⁷¹.

Fe₃O₄ nanoparticles. Known amounts of FeCl₃·6H₂O (0.605 g) and FeCl₂·4H₂O (0.215 g) were dissolved in deionized water. Then, the obtained solution was placed in an ultrasonic homogenizer for 5 min. After that, 60 mL of 1 M NaOH was added dropwise into solution under ultrasonic at 70 °C. After 60 min, the brownish powder was obtained at a pH of 13.4 and it was separated from the solution using a centrifuge. Finally, it was calcined at 300 °C for 1 h⁷².

ZrO₂/TiO₂/Fe₃O₄ nano-photocatalyst. ZrO₂/TiO₂/Fe₃O₄ photocatalysts were prepared using solid-state dispersion method. ZrO₂, TiO₂, and Fe₃O₄ nanoparticles were mixed at a ratio of 4:8:1 in ethanol solution. The resultant ternary oxide was stirred at a constant rate of 300 rpm for 15 min. Then, ethanol was removed from a mixture of nanocomposite by evaporation. Then, the product was dried at 110 °C and calcined at 450 °C for 6 h to obtain ZrO₂/TiO₂/Fe₃O₄ nanocomposite photocatalyst⁶⁰. The mixing ratio of used components in the synthesized nanocomposite was selected based on the highest efficiency of naproxen degradation under the same operation conditions. The best ratio was achieved (4:8:1) of the ZrO₂, TiO₂, Fe₃O₄ compounds.

Photocatalyst characterization. The mineralogical analysis of the prepared nanoparticles was characterized by X-ray diffraction (Inel France, Equinox 3000) with Cu $K\alpha$ radiation. SEM(AIS2100). It was used to determine the surface morphology and microstructure of ZrO₂/TiO₂/Fe₃O₄ nanocomposite photocatalyst. The Fourier-transform infrared spectroscopy (VERTEX 70, Bruker, USA) in the wavelength range from 400 to 4000 cm⁻¹ was used to analyze the chemical bonding in a photocatalyst. Texture properties of nanoparticles was investigated using TriStar-II-Series, Micromeritics Instrument Corporation, USA. The specific surface area of photocatalysts was determined via the N₂ adsorption–desorption and Brunauer–Emmett–Teller (BET) model. Barrett–Joyner–Halenda (BJH) method was used to calculate the size of pores and pore size distribution using adsorption–desorption curves. Powder samples for XPS analysis are prepared in the form of pellets in the laboratory (the powder should be large enough to cover a surface of 1.5 × 1.5 cm), then the samples should be placed in a vacuum chamber after preparation. A PHI Perkin-Elmer Model 5400 instrument was used to record XPS spectra. The EELS analysis was obtained using a sub-nanometer probe size using the GIF2000 Filter. The PL Spectroscopy was recorded by Avaspec-2048-TEC model spectrometer.

Point of zero charge determination. An amphoteric oxide method was used to determine the point of zero charge of the photocatalyst⁷³. In order to determine the point of zero charge (PZC), 0.25 g of the synthesized photocatalyst was added into the solution with the same ionic strength and different pH values. The synthesized nanocatalyst was added to 50 mL of 0.1 M NaNO₃ solution. The pH of solution was adjusted in the range of 3–9 using 0.1 M H₂SO₄ and 0.1 M NaOH. The pH of solution was measured before and after 24 h mixing and those were called pH_i and pH_f respectively. The plot of pH changes (Δ pH) as a function of initial pH_i was used for the determination of PZC⁷³.

Optimization of the photocatalyst Activity. In order to optimize photocatalyst activity, the RSM has been used. Design Expert 8.0 software (Stat-Ease, Inc., USA) was used to design experiments and analyze mathematical modeling. Each experiment was performed in duplicate. Box–Behnken design (BBD) was applied in this

Factor	Name	Units	Minimum	Maximum	Coded low	Coded high
A	NPX concentration	mg/L	10.00	30.00	-1 ↔ 10.00	+1 ↔ 30.00
B	Time	Min	30.00	90.00	-1 ↔ 30.00	+1 ↔ 90.00
C	pH	-	3.00	9.00	-1 ↔ 3.00	+1 ↔ 9.00
D	Catalyst concentration	g/L	0.1000	0.5000	-1 ↔ 0.10	+1 ↔ 0.50

Table 2. Operating parameters for degradation of naproxen experiment.

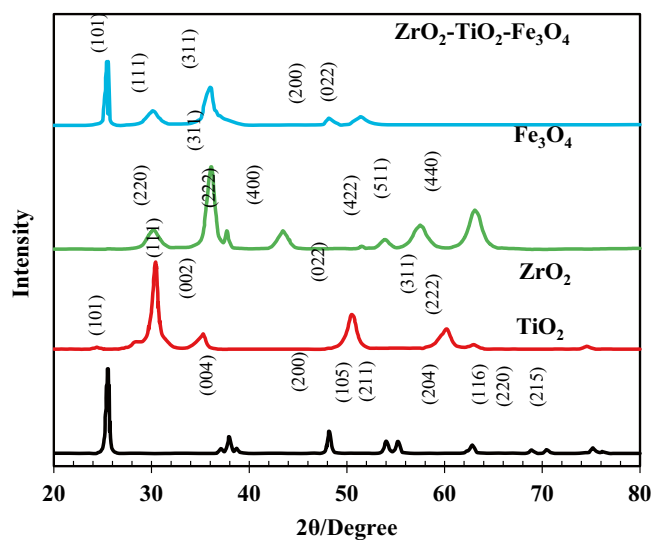


Figure 1. The XRD patterns of ZrO_2 , TiO_2 , Fe_3O_4 , and $ZrO_2/TiO_2/Fe_3O_4$ nanocomposite.

study because of its rotatable or nearly rotatable second-order design. The “y” was the response (the percentage of naproxen degradation). We evaluated four independent variables, including catalyst loading dosage, initial concentration of naproxen, time and pH value in order to find an optimal condition:

$$y = f(x_1, x_2, x_3, x_4) \quad (1)$$

Photocatalyst activity. $ZrO_2/TiO_2/Fe_3O_4$ Photocatalyst was used for the degradation of naproxen in a pharmaceutical synthetic solution. The experiments were conducted based on the conditions in Table 2. In this study, the effects of solution pH, time, initial naproxen concentration, and photocatalyst loading dose on naproxen degradation were evaluated. To determine the adsorption behaviour of the photocatalyst, the solution kept was in the dark for half an hour. The reactor was irradiated immediately after adding the photocatalyst. For each experiment, a 150 W UV light source has been used for irradiation (The intensity was kept as 15 W/m^2). At the end of each experiment, centrifugation with 12,000 rpm for 20 min have been performed for each withdrawn sample followed by absorbance measurement using UV-Vis (Shimadzu UV2401PC) at $\lambda = 230 \text{ nm}$. The efficiency of designed photocatalysts for the degradation of naproxen was calculated as follows:

$$NPXR(\%) = \left(\frac{C_i - C_f}{C_i} \right) \times 100 \quad (2)$$

where C_i and C_f are the naproxen concentration before and after degradation reaction respectively.

Reusable photocatalytic properties. Reusability tests were conducted for $ZrO_2/TiO_2/Fe_3O_4$ Photocatalyst. Briefly, the selected photocatalyst being used in the degradation test of naproxen was separated from solution using a 1.3 Tesla magnet. Used photocatalysts were rinsed in distilled water and irradiated under UV light for 12 h. In order to evaluate the reusability of a photocatalyst, seven successive experimental runs were conducted.

Results and discussion

Characterization. *XRD analysis.* The constituting phase, crystalline size, and crystalline structures of the ZrO_2 , TiO_2 , and Fe_3O_4 , nanoparticles, and $ZrO_2/TiO_2/Fe_3O_4$ nanocomposite characterized using XRD, which are depicted in Fig. 1. For ZrO_2 , the primary characteristic diffraction peaks appeared at $2\theta = 30^\circ, 35^\circ, 50.8^\circ, 60.1^\circ,$ and 63° were corresponds to crystal planes of (1 1 1), (0 0 2), (0 2 2), (3 1 1), and (2 2 2). The majority of these

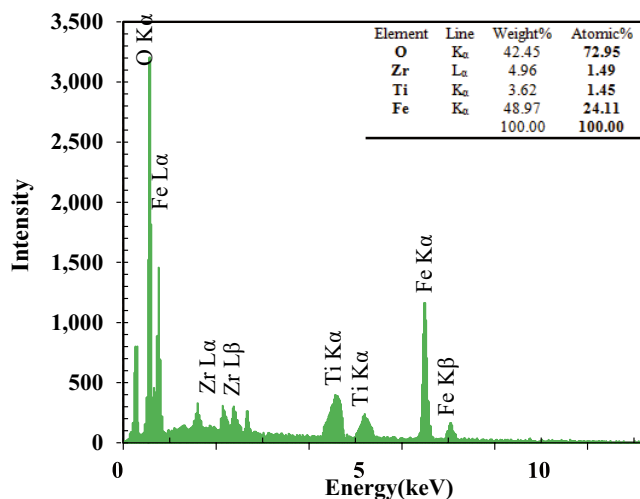


Figure 2. EDX spectrum. (Insert: Element analysis of synthesized nanocomposite).

crystalline phases are monoclinic. The transition from tetragonal to monoclinic can occur with an increase in the calcination temperature which increases the crystallite size of the samples⁷⁴. According to Fig. 1 for TiO₂ sample, there is good agreement between the results of this study and the XRD pattern for the titanium dioxide phase reported in the literature^{75–77}. The diffraction peaks at 2 theta values of 25.32°, 37.90°, 48.09°, 54.10°, 55.15°, 62.85°, 68.99°, 70.49°, and 75.12° were belonged to crystal planes of (1 0 1), (0 0 4), (2 0 0), (1 0 5), (2 1 1), (2 0 4), (1 1 6), (2 2 0), (2 1 5)⁷⁸. All the peaks observed in the diffraction pattern of TiO₂ nanoparticles are in good agreement with anatase (JCPDS No. 00–001-0562). Figure 1 clearly shows magnetite formation with well-defined crystallinity in Fe₃O₄. All of the diffraction peaks are related to (2 2 0), (3 1 1), (2 2 2), (4 0 0), (4 2 2), (5 1 1), and (4 4 0) crystal planes and those were belonged to Fe₃O₄. The results confirmed the occurrence of inverse spinel structure in Fe₃O₄. The XRD peaks of impurities were not observed, which means that the synthesized Fe₃O₄ nanoparticles are pure⁷⁹. Finally, in the XRD pattern of ZrO₂/TiO₂/Fe₃O₄ nanocomposite, the main peaks related to all three compounds were observed. The results showed that the sample has spinel reverse cube of Fe₃O₄ structure. The ZrO₂ is amorphous phase and the phase of TiO₂ is tetragonal (Anatase). The average crystallite sizes were calculated by Scherrer formula:

$$D = \frac{0.9 \times \lambda}{\beta \times \cos \theta} \quad (3)$$

where λ is X-ray wavelength, β is the full width at half maximum of the diffraction line and θ is the diffraction angle⁸⁰. The average crystallite size of TiO₂, ZrO₂, Fe₃O₄ and ZrO₂/TiO₂/Fe₃O₄ was found to be 18.75 nm, 22.29 nm, 13.27 and 33.42 nm respectively. The most important cause of difference in particle size of synthesized samples can be the difference in their synthesis method⁸¹.

EDX analysis. EDAX analysis confirmed the presence of all elements, including Zr, Ti, O and Fe in the synthesized photocatalyst and there is no evidence of any other element. The inserted table in Fig. 2 presents an elemental composition of the photocatalyst. The results showed that the atomic ratio of Zr:Ti:Fe was 0.42:2.08:1.00. The synthesized nanocomposite had different peaks at 0.70, 6.39, and 6.92 keV which are related to L α , K α , and K β of Fe and 0.52 keV is K α of oxygen. Peaks at 2.04 (L α) and 2.26 (L β) keV are for zirconium. Fe₃O₄ particles are larger than TiO₂ particles based on the results obtained.

SEM analysis. SEM analysis was used to determine the morphology and size of nanoparticles of ZrO₂/TiO₂/Fe₃O₄ nanocomposite (see in Fig. 3). In Fig. 3, ZrO₂ and TiO₂ nanoparticles are almost cubic and spherical respectively, while Fe₃O₄ does not have a specific shape.

BET analysis. Figure 4a and b show the porosity distribution curve and pore size distribution of ZrO₂/TiO₂/Fe₃O₄ nanocomposite. The specific surface area (SSA) was calculated using the N₂ isotherms. The BET-SSA, the volume of pores, the average size of pores of the photocatalyst obtained were 280 m²/g, 0.92 cm³/g, and 42 nm respectively. The sample is mesoporous as the diameter of pores is larger than 2 nm. Hysteresis loop of types IV-H1 was obtained for the sample which is related to cylindrical and spherical pores in the sample⁸². In terms of pore size distribution, wide pore size distribution was observed, especially, pores with size larger than 3 nm had significant volume in the sample. It was found that the pore size larger than 3 nm is appropriate for the reactants penetration into the porous media of photocatalyst^{83,84}.

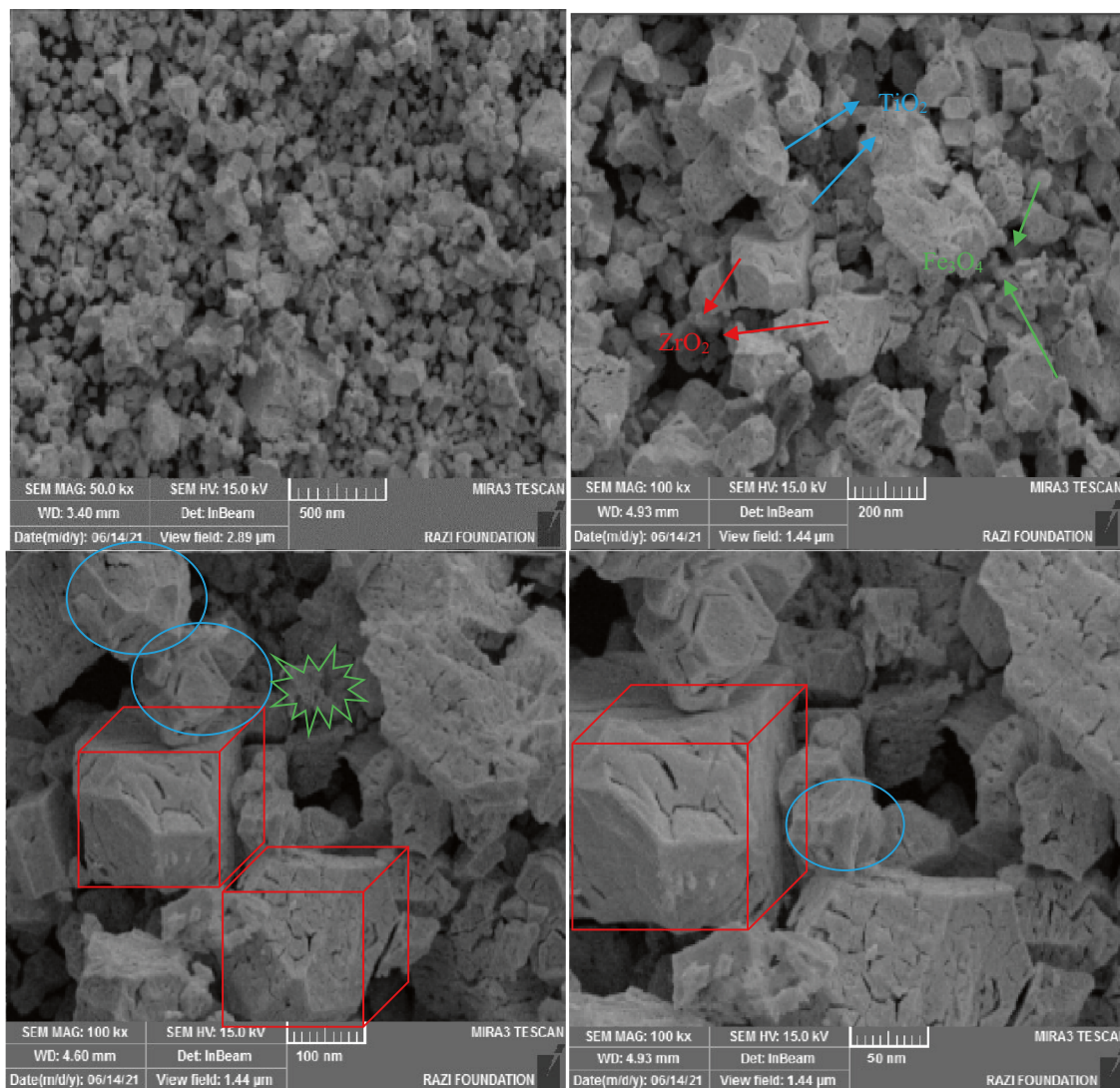


Figure 3. SEM image of $ZrO_2/TiO_2/Fe_3O_4$ nanocomposite.

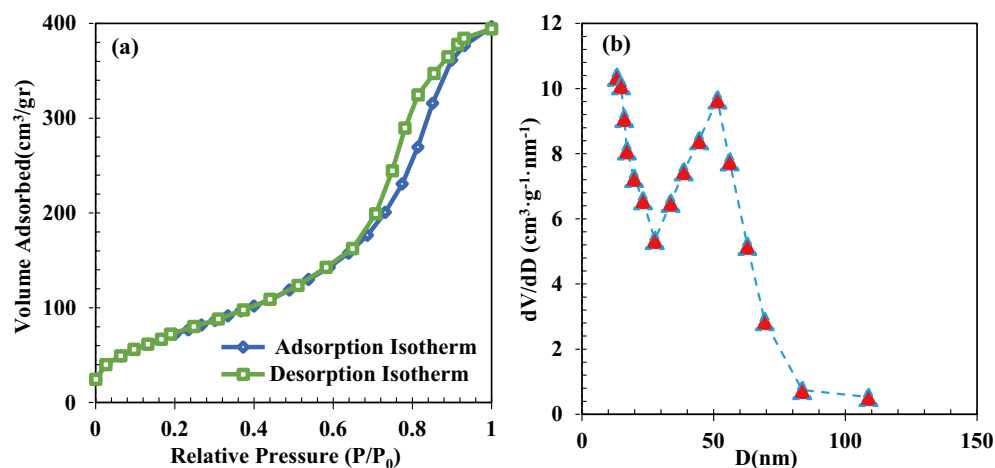


Figure 4. (a) N_2 adsorption–desorption hysteresis and (b) pore size distribution of $ZrO_2/TiO_2/Fe_3O_4$ photocatalyst.

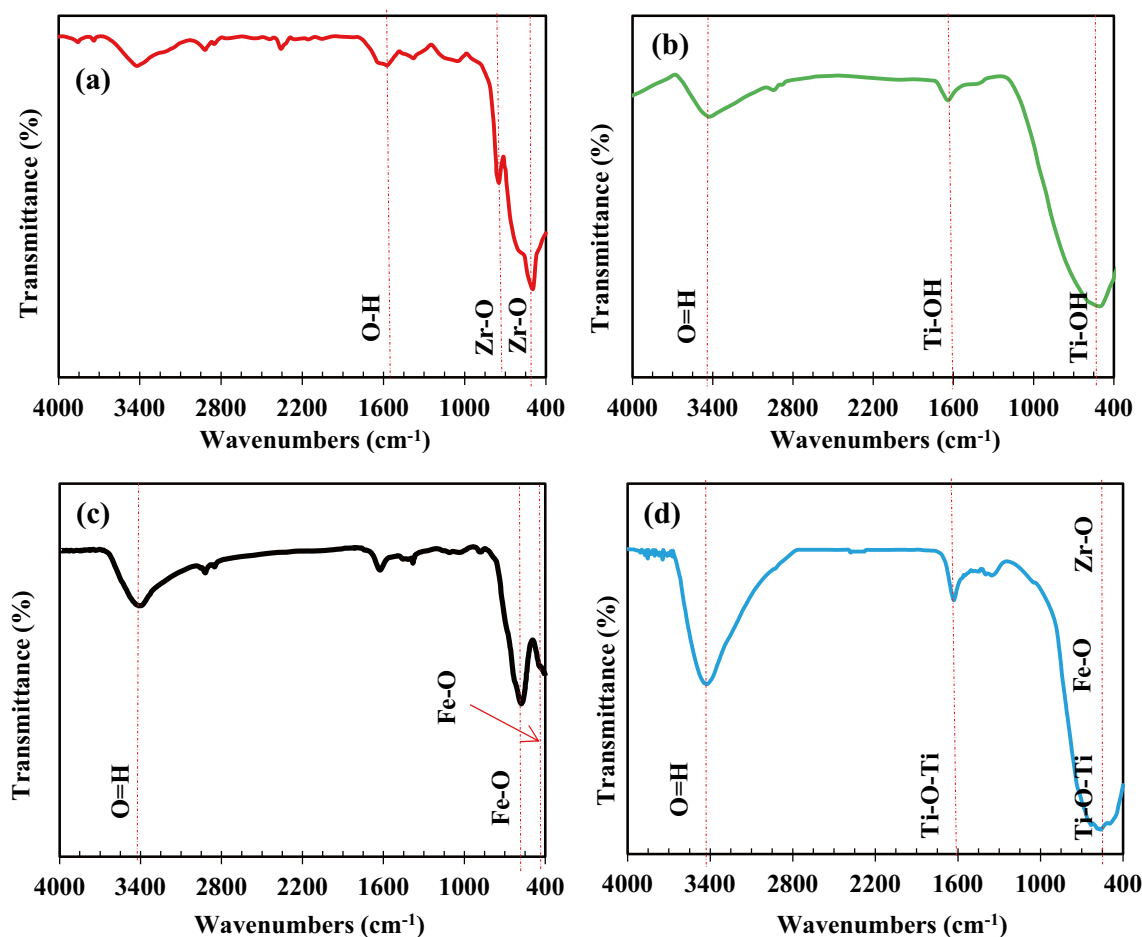


Figure 5. FTIR spectra of (a) ZrO_2 , (b) TiO_2 , (c) Fe_3O_4 , (d) of $\text{ZrO}_2/\text{TiO}_2/\text{Fe}_3\text{O}_4$ photocatalyst.

FTIR analysis. Figure 5a–d shows the FTIR analysis of ZrO_2 , TiO_2 , Fe_3O_4 , and $\text{ZrO}_2/\text{TiO}_2/\text{Fe}_3\text{O}_4$ photocatalysts. As for ZrO_2 , the strong broad peak at $498\text{--}502\text{ cm}^{-1}$ region is attributed to the vibration mode of ZrO_3^{2-} groups. The peaks around 754 cm^{-1} are related to the Zr–O stretching vibrations in ZrO_2 . The IR at 1553 cm^{-1} attributed to stretching of O–H groups, which indicates the adsorbed moisture⁸⁵. For TiO_2 nanoparticles, TiO_2 network bonds and deformation vibrations of stretching mode of Ti–OH peaks were observed at 483 cm^{-1} and 1623 cm^{-1} respectively. It can be related to the absorption of water on the TiO_2 surface. Asymmetrical and symmetrical stretching vibration of hydroxyl groups (–OH) was observed at 3405 cm^{-1} . The obtained results are consistent with those reported in the literature^{86,87}. According to Fig. 5c, the stretching vibration of the O–H can be attributed to the absorption band 3444 cm^{-1} . The peaks at 419 cm^{-1} and 589 cm^{-1} were attributed the stretching vibration of the Fe–O. The strong peaks in the $450\text{--}700\text{ cm}^{-1}$ range were attributed to stretching vibrations of Zr–O, Ti–O, and Fe–O in $\text{ZrO}_2/\text{TiO}_2/\text{Fe}_3\text{O}_4$ photocatalyst. The results confirm the presence of all three nanoparticles in the $\text{ZrO}_2/\text{TiO}_2/\text{Fe}_3\text{O}_4$ photocatalyst.

XPS analysis. For further investigation of the nature of the synthesized nanomaterial, we performed high-resolution X-ray photoelectron spectroscopy (XPS) on the synthesized ZrO_2 , TiO_2 and Fe_3O_4 pure nanoparticles and the $\text{ZrO}_2/\text{TiO}_2/\text{Fe}_3\text{O}_4$ nanocomposite. The XPS spectra of pure and nanocomposite samples are shown in Fig. 6. Figure 6a and b show the XPS results of high-resolution Fe_3O_4 nanoparticles. Three components of the Fe–O bond can be seen in the XPS spectrum. After photoexcitation, the splitting of O1s at 531.6 eV indicates the formation of a Fe–O bond. The XPS peak of C1s at 292.6 eV and O1s at 531.6 eV indicate the formation of Fe–C and Fe–O bonds following particle photoexcitation (see Fig. 6a and b)⁸⁸. Figure 6c and d show the XPS analysis of the pure TiO_2 elemental composition. According to the XPS spectrum, elements Ti, C, and O are present on the surface of the TiO_2 nanoparticles. Fe_3O_4 and TiO_2 nanoparticle samples contained carbon resulting from carbon-based contaminants. The XPS peaks of Fig. 6c show C1s at 288.27 eV and O1s at 532.1 eV and Ti2p at 461.1 eV . Figure 6d shows the peaks of 458.5 eV and 464.2 eV , which correspond to Ti 2p3/2 and Ti 2p1/2, respectively. The peak position between Ti 2p3/2 and Ti 2p1/2 at 464.2 eV indicates the presence of Ti^{4+} oxidation state^{89,90}. Figure 6e and f show the XPS spectrum of ZrO_2 nanoparticles, which indicate the presence of relevant elements. The Zr3d level spectra of Fig. 6f show the Zr3d5/2 and Zr3d3/2 peaks at binding energies of 185.66 eV and 188.1 eV , respectively. The energy difference of 2.44 eV between the two peaks indicates the presence of Zr^{4+} ⁹¹. The third suitable peak for the shoulder that appears at the base of Zr 3d3/2 can be attributed to the lack of oxygen, which can be due to under-coordinated Zr sites of very small ZrO_2 nanoparticles⁹². XPS

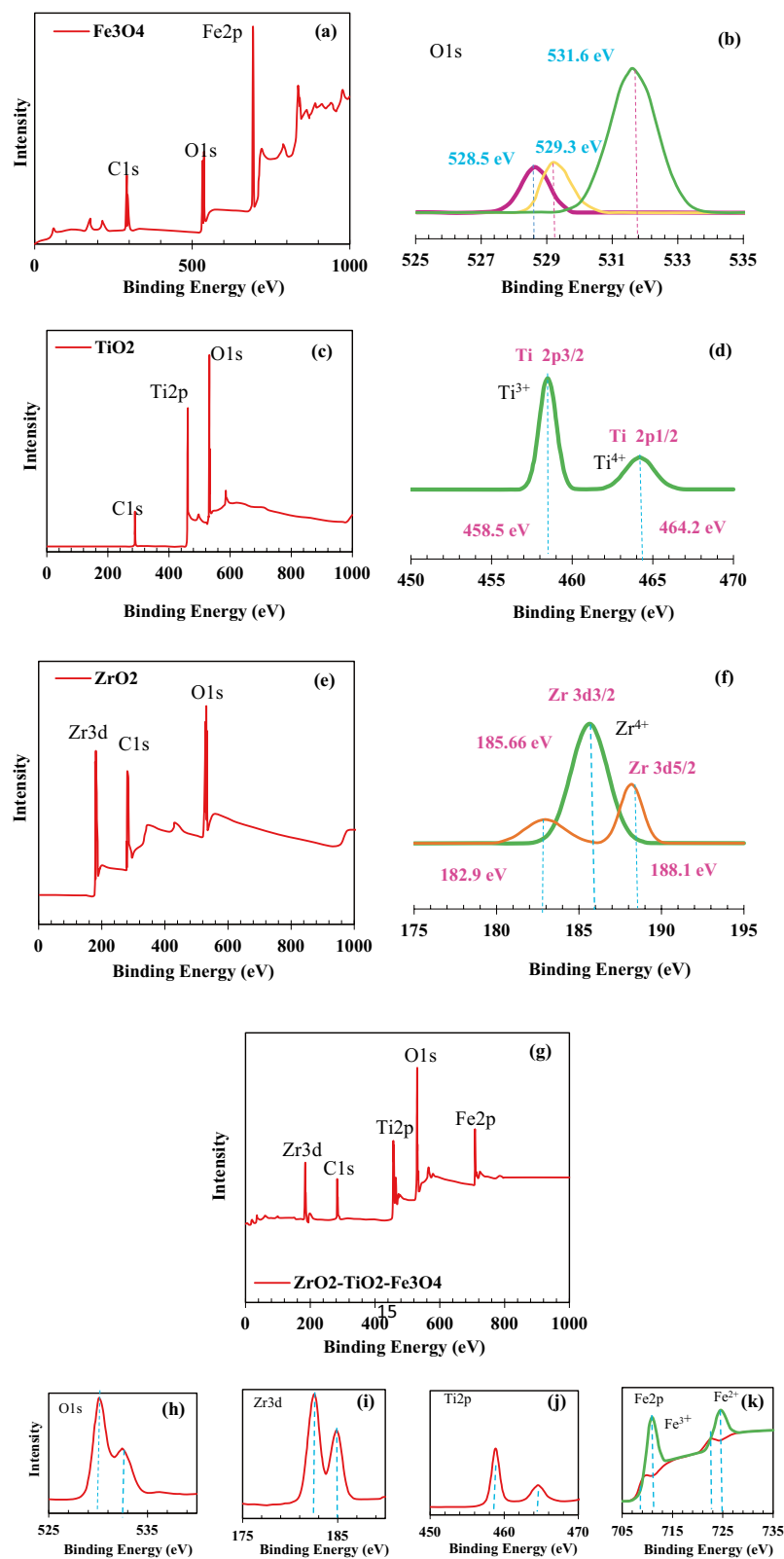


Figure 6. XPS analysis of Nanoparticles (a) Fe₃O₄, (b) The O1s level spectrum, (c) TiO₂, (d) The Ti 2p level spectrum, (e) ZrO₂, (f) The Zr 3d level spectrum, and (g) Nanocomposite of ZrO₂/TiO₂/Fe₃O₄, XPS spectrum of (h) The O1s level (i) The Zr 3d level (j) The Ti 2p level and (k) The Fe 2p level.

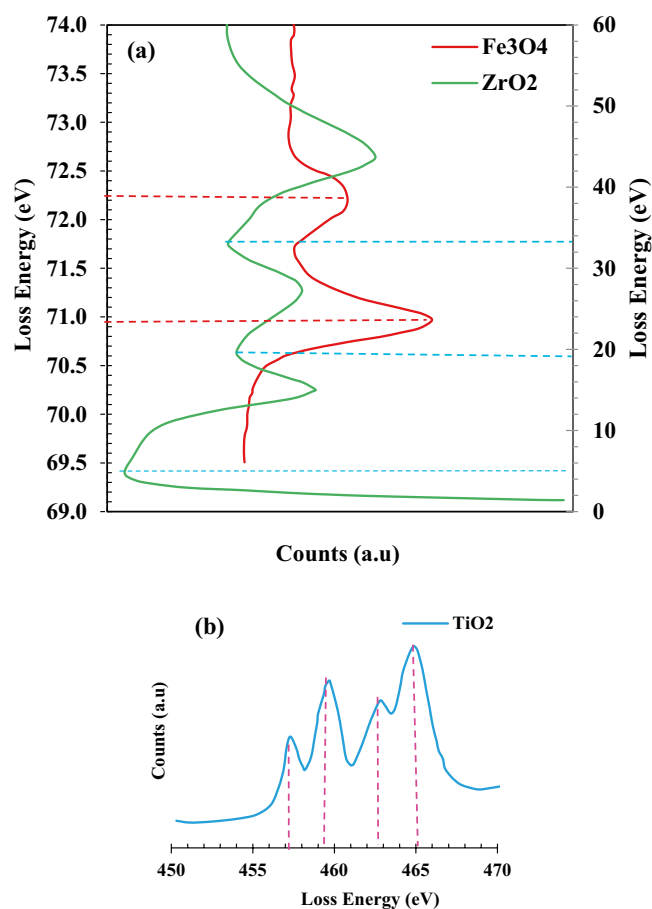


Figure 7. EELS spectrum for Structures of (a) Fe_3O_4 , (b) ZrO_2 and TiO_2 .

analysis was investigated to accurately determine the surface composition and chemical state of $\text{ZrO}_2/\text{TiO}_2/\text{Fe}_3\text{O}_4$ nanocomposite (As shown in Fig. 6g–k). As shown in Fig. 6g, the major peaks of Zr3d, C1s, Ti2p, O1s, and Fe2p are shown at 184.33, 282.59, 458.05, 530.18, and 708.37 eV, respectively. These results, in addition to confirming the presence of three nanoparticles ZrO_2 , Fe_3O_4 and TiO_2 , showed that ZrO_2 , Fe_3O_4 and TiO_2 are mainly present as separate phases in the $\text{ZrO}_2/\text{TiO}_2/\text{Fe}_3\text{O}_4$ composite. Figure 6h shows that the binding energy of O1s appears at 530.08 eV, which proves the existence of oxygen in the crystal lattice (O_2)⁹³. In Fig. 6i, the dual peaks of Zr 3d with binding energies at 182.52 eV and 184.87 eV correspond to the chemical states Zr 3d3/2 and Zr 3d5/2, respectively, indicating zirconium in the +4 oxidation state⁹⁴. In addition, two peaks at 182.52 and 184.87 eV indicate the presence of Zr-Ti chemical bonds in the composites⁹⁵. In Fig. 6j, the Ti 2p peaks at 458.84 eV and 464.58 eV correspond to the chemical states Ti 2p1/2 and Ti 2p3/2, respectively. Ti peaks confirm the presence of Ti^{4+} oxidation state in the nanocomposite. Meanwhile, the peak of 464.58 eV can be attributed to Zr-Ti chemical bonds⁹⁶. The presence of chemical bonds Fe–O, Zr–O, Ti–O and Zr–Ti, Ti–Fe and Zr–Fe indicates a phase contact between Fe_3O_4 , TiO_2 and ZrO_2 . In Fig. 6k for Fe_3O_4 , the major peaks at 710.96 eV and 724.59 eV are attributed to Fe^{3+} 2p3/2 and Fe^{3+} 2p1/2, respectively. The bond energy of Fe^{2+} 2p3/2 and Fe^{2+} 2p1/2 has a dual peak at 708.96 eV and 721.52 eV, respectively. Results of Fe_3O_4 XPS analysis are consistent with Fe2p spectrum⁹⁷.

EELS analysis. The electron energy-loss spectroscopy (EELS) analysis was used to identify the pure samples more accurately. The combination of EELS and statistical analysis can provide more information on the differentiation of Fe_3O_4 and Fe_2O_3 spinel structures. Figure 7a shows that the energy-loss peaks at 70.96 eV and 72.19 eV can only be attributed to Fe_3O_4 phase, since the expected value for gamma- Fe_2O_3 (70.2 eV) is significantly different. As shown in Fig. 7a, the EELS spectra of ZrO_2 nanoparticles are obtained (obtained peaks for ZrO_2 are 1.4, 14.8, 27.28 and 43.72 eV respectively). The synthesized ZrO_2 nanoparticles can be proved according to the obtained peaks from the analysis. As shown in Fig. 7, the Ti structure in the EELS spectrum for Ti^{4+} , indicates a lower oxidation state which has edges shift slightly towards the lower energy loss. Here, the blue curve is the fine structure of the Ti^{4+} state. EELS was obtained using a sub-nanometer probe size using the GIF2000 Filter.

Photoluminescence spectra. The light absorption of photocatalysts significantly affects the activity of photocatalysts. Also, the spectrum of PL (Photoluminescence) and their intensity are closely related to its photocatalytic activity. Figure 8a–d shows the photoluminescence spectra (PL) of pure ZrO_2 , TiO_2 and Fe_3O_4 samples and the

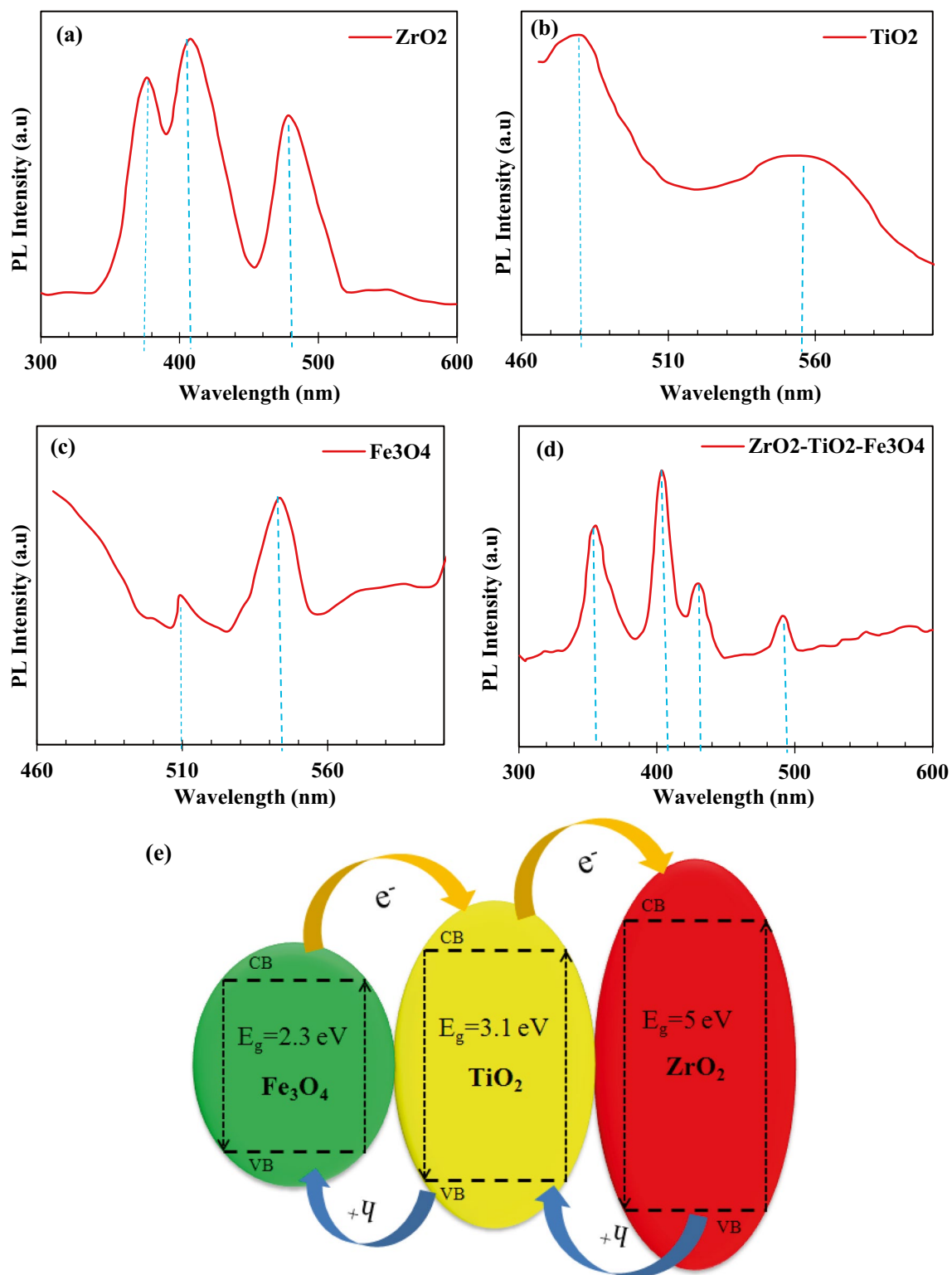


Figure 8. Photoluminescence (PL) spectra of (a) ZrO₂, (b) TiO₂, (c) Fe₃O₄ nanoparticles and (d) ZrO₂/TiO₂/Fe₃O₄ nanocomposite, (e) Energy level and electron–hole pair separation/transfer in ZrO₂/TiO₂/Fe₃O₄ nanocomposite.

ZrO₂/TiO₂/Fe₃O₄ nanocomposite at room temperature in the wavelength range of 300–600 nm with an excitation wavelength of 293 nm. As shown in Fig. 8a–c the pure ZrO₂, TiO₂ and Fe₃O₄ samples show significant PL signals at 376, 407, 478, and 480, 556, 509 and 543 nm, respectively. Among all samples, the TiO₂ sample shows the highest intensity. The obtained PL spectrum for pure ZrO₂ nanoparticles is almost similar to the results previously reported⁹⁸. According to previous research^{99–102}, the presence of these peaks in the visible range is probably due to the presence of oxygen vacancies, defects, surface states and other structural impurities. A high PL intensity of pure ZrO₂ appears to indicate that the ZrO₂ surface states are much lower, hence easy electron transfer can occur between VB and CB of ZrO₂ even with a low-energy laser excitation source (325 nm)¹⁰³. Additionally, when Fe₃O₄ and TiO₂ are loaded with ZrO₂ as ternary oxide catalysts, the PL intensity of ZrO₂ decreases abruptly (Fig. 8d). The formation of a chemical interaction between pure oxides when they accumulate together (–Ti–O–Fe–), (–Ti–O–Zr–) and (–Fe–O–Zr–), as shown, has a profound effect on the photocatalytic properties¹⁰⁴. A PL spectrum of the physically mixed pure ZrO₂, TiO₂, and Fe₃O₄ catalysts in different ratios further confirms the synergistic effect of the ZrO₂/TiO₂/Fe₃O₄ ternary system and the presence of (–Ti–O–Fe–), (–Ti–O–Zr–) and (–Fe–O–Zr–). The peaks shown at 403, 427, and 490 nm under the excitation wavelength of 293 nm for the ZrO₂/TiO₂/Fe₃O₄ nanocomposite must be due to the interference of trap states between the gaps, such as surface defects and oxygen vacancies (Fig. 8d)¹⁰⁵. Preparation for solid samples (powder) was performed for PL (Photoluminescence Spectroscopy) analysis. The PL Spectroscopy was recorded by Avaspec-2048-TEC model spectrometer. The valence band (VB) and conduction band (CB) are shown in Fig. 8e. In this figure, the photocatalyst energy bands of Fe₃O₄/TiO₂/ZrO₂ are shown in (CB) and (VB). The VB determines the energy levels of electrons in the VB of an atomic structure. The combination of three metal oxides can be improved electromagnetic separation and narrowing of the photocatalyst band gap. In Fe₃O₄/TiO₂/ZrO₂ semiconductor, electrons migrate to CB whereas; positive holes are created on VB. The OH is formed through the reaction of charge carriers with adsorbed compounds on the photocatalyst surface. In Fe₃O₄/TiO₂/ZrO₂ nanocomposite, the electron–hole separation may occur between ZrO₂ and TiO₂. The surface energy of Fe₃O₄ for VB and CB was placed in TiO₂ band gap and surface energy of TiO₂ was placed in ZrO₂ band gap (Fig. 8e). In the excitation of electrons from three catalysts, the majority of electrons migrate from CB of ZrO₂ to CB of TiO₂, then to CB of Fe₃O₄. As a result, electron–hole recombination is prevented in ZrO₂ and occurs in Fe₃O₄.

Photocatalyst performance. The experimental work was designed and the obtained actual results, as well as predicted values, were provided in Table 3. Box–Behnken design for RSM was used for the experimental design. Statistical investigation of experimental data was performed using linear, two-factor interaction, quadratic, and cubic models. The results were given in Table 4. According to Table 4 and R² values, the quadratic model was found the most accurate model for the prediction of experimental data in terms of naproxen removal. Its predicted R² value was found to be 0.9901 which means the developed model equation is able to predict the results accurately. Therefore, the following quadratic polynomial model in terms of coded factors was proposed for investigation of naproxen degradation from pharmaceutical synthetic solution as a function of operating parameters:

$$\begin{aligned} \text{Sqrt}(\text{NaproxenRemoval}) = & -0.2384A + 0.1918B - 0.1575C \\ & + 0.3590D - 0.0130AB - 0.0836AC \\ & + 0.0471AD + 0.0192BC - 0.0091BD \\ & - 0.0204CD - 0.1389A - 0.1168B - 0.2035C + 0.1610D \end{aligned} \quad (4)$$

where A, B, C, D are photocatalyst dose (g/L), time (min), solution initial pH, and initial concentration of naproxen (mg/L). The variables were defined at three levels including –1, 0, and +1.

Figure 9 illustrates the individual effects of operational parameters on naproxen removal. The contour lines represent lines of equal response and can be visualized as response contours two factors at a time. In this study, contour lines mean the performance of photocatalyst for naproxen removal at different operating parameters. The contour map reflects the cross-interaction between two variables by keeping the other variable constant. Interaction of initial pH and naproxen concentration for photocatalyst dose of 0.3 g/L and time of 60 min was shown in Fig. 9a. At a pH value of 6, increasing the initial concentration of naproxen from 10 to 30 mg/L led to the reduction of naproxen removal from 91.81 to 82.9%. Naproxen removal is reduced due to solution turbidity and a decrease in light absorption by the photocatalyst. Also, the amount of hydroxyl radical in the solution decreases. Furthermore, the photocatalyst surface is covered by pollutants with increasing its concentration from 10 to 30 mg/L which decreases photon penetration into the photocatalyst. Therefore, the photocatalyst was unable to generate enough electron–hole pairs, resulting in a reduced removal of naproxen. In the interaction between time and initial pH of the solution (Fig. 9b), the photocatalyst dosage and initial concentration of naproxen were considered 0.3 g/L and 20 mg/L respectively. Firstly, the efficiency of naproxen degradation was increased from 90.10 to 91.34% with increasing pH of the solution from 3 to 6, then, it was decreased to 84.9% at a pH value of 9. These changes are related to the oxidation potential and surface charge of the photocatalyst. The pH of the media can have a significant impact on the adsorption and desorption of pollutants on the photocatalyst surface.

The amount of pK_a is 4.15 for the naproxen. At pH values higher than 4.15, naproxen has a negative charge, otherwise, it has a positive charge. The neutral charge point of photocatalyst is 6. Therefore, it has a positive charge at pH below 6, whereas the surface charge of photocatalyst is negative at pH above 6. When the pH value is between 4.15 and 6, the naproxen and photocatalyst have opposite charges, so the adsorption of naproxen on the photocatalyst surface increases in this range. It is for this reason that maximum degradation occurs at pH 6 rather than pH 3 or 9. When the pH solution was 6, an increase in time from 30 to 60 min increased naproxen removal from 84.10 to 91.34%. The time and photocatalyst dosage interaction at constant initial pH and concentration

Run	Factor 1	Factor 2	Factor 3	Factor 4	Response	
	A:NPX concentration	B:Time	C:pH	D:catalyst concentration	Naproxen Removal	
	mg/L	min	–	g/L	Actual Value	Predicted Value
					%	%
1	10	90	3	0.1	87.3	87.6
2	10	90	9	0.5	96.8	97.2
3	30	90	9	0.1	72.1	72.8
4	10	60	6	0.3	92.3	91.8
5	20	60	3	0.3	88.8	89.1
6	20	60	6	0.3	89.8	89.9
7	20	60	6	0.3	90.5	89.9
8	20	60	6	0.3	89	89.9
9	30	90	3	0.5	95.4	95.3
10	20	60	6	0.1	86.8	86.1
11	30	30	9	0.5	79.2	79.2
12	10	30	9	0.5	88.9	88.9
13	10	30	3	0.5	93.5	93.1
14	10	90	3	0.5	100	100
15	20	60	6	0.3	89.6	89.9
16	30	30	9	0.1	66.1	65.8
17	30	30	3	0.1	73.8	73.8
18	10	30	9	0.1	77.5	77.8
19	30	90	3	0.1	79.9	79.7
20	30	30	3	0.5	89.6	89.5
21	30	60	6	0.3	82.8	83.0
22	10	30	3	0.1	80.5	80.5
23	10	90	9	0.1	86.5	86.3
24	20	60	6	0.3	90.2	89.9
25	20	60	6	0.3	89.3	89.9
26	30	90	9	0.5	86.3	86.1
27	20	30	6	0.3	83.8	84.1
28	20	60	9	0.3	83.8	83.2
29	20	60	6	0.5	99.8	100
30	20	90	6	0.3	92.1	91.4

Table 3. Operational parameters range in the designed experiments and actual and predicted results in terms of naproxen removal. Significant values are in bold.

Source	Sequential p -value	Lack of fit p -value	Adjusted R^2	Predicted R^2	
Linear	< 0.0001	0.0002	0.8158	0.7680	
2FI	0.6041	0.0002	0.8050	0.5781	
Quadratic	< 0.0001	0.5274	0.9952	0.9901	Suggested
Cubic	0.5874	0.3447	0.9948	0.9248	Aliased

Table 4. Statistical investigation based on linear, two-factor interaction, quadratic, and cubic models. Significant values are in bold.

of naproxen of 6 and 20 mg/L was shown in Fig. 9c. In Fig. 9c, and for a 60-min experiment run, there was an increase in naproxen degradation from 86.2 to 100% when the photocatalyst dosage was increased from 0.1 to 0.5 g/L. Photocatalyst dosage had a significant effect on naproxen degradation, increasing the number of available active sites for the generation of hydroxyl radicals. However, too much photocatalyst in the system can reduce naproxen degradation as a result of agglomeration of photocatalyst nanoparticles. The reduction in active site of the photocatalyst resulted from agglomeration. It was found that a decrease in pH can increase naproxen degradation (Fig. 9d), and the greatest degradation was obtained at pH 3. The solution pH had a complicated effect on the photocatalytic oxidation reaction. The optimum pH value is highly dependent on the type of pollutant and point of zero charges (PZC) of the photocatalyst. According to Fig. 10, it is 6 for the synthesized photocatalyst. At $\text{pH} = \text{pH}_{\text{PZC}}$, the surface charge is neutral. The surface charge can be positive or negative at $\text{pH} < \text{pH}_{\text{PZC}}$ and

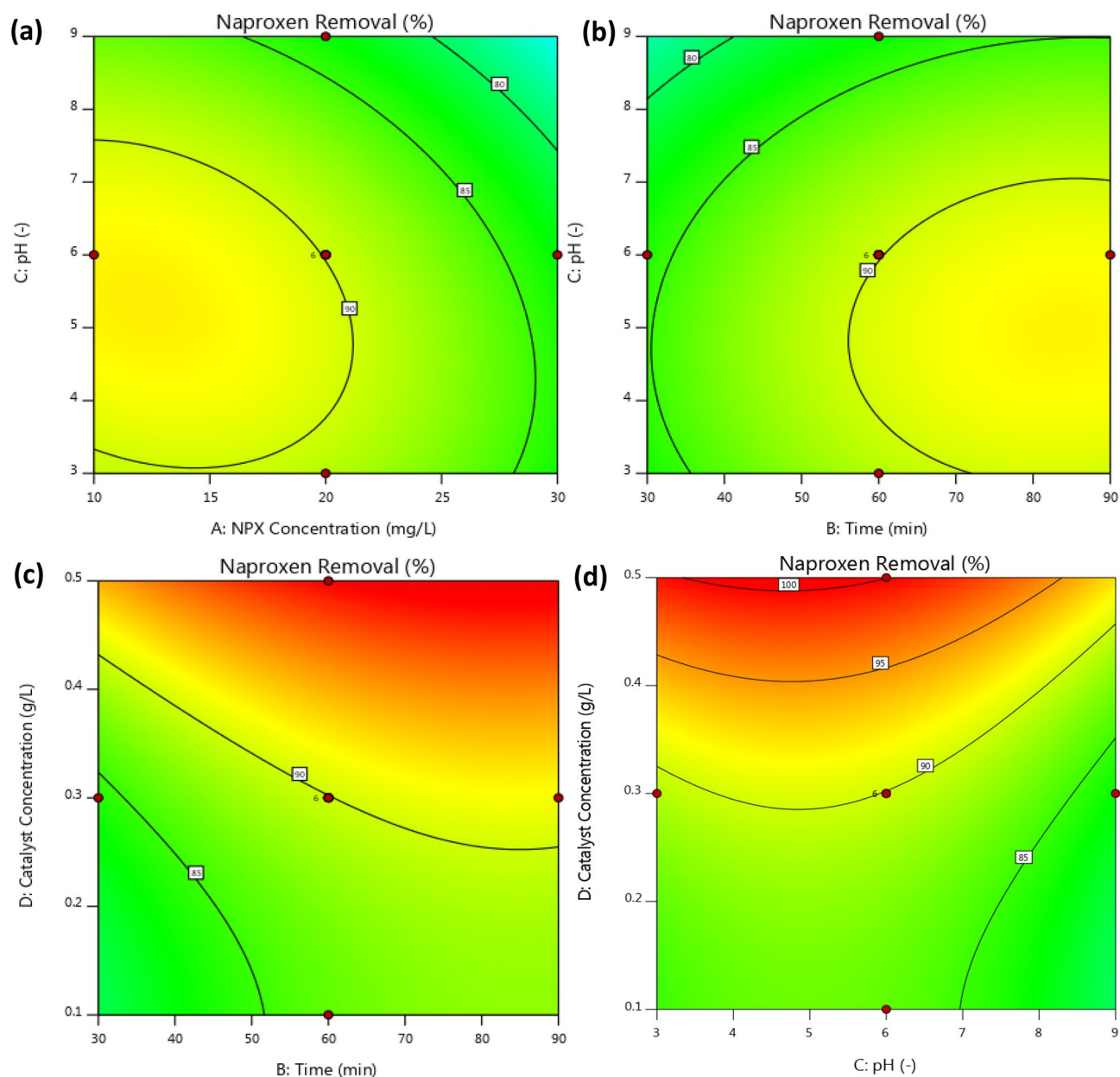


Figure 9. The 2D contour plots of RSM for investigation the degradation percentage of naproxen.

$\text{pH} > \text{pH}_{\text{PZC}}$. The amount of adsorption is highly dependent on the surface charge of photocatalyst and pollutant and it can be controlled by a change in solution pH.

The analysis of variance (ANOVA) results obtained for the present model are summarized in Table 5. The results suggested that a quadratic model is significant because of its high F-value (431.34) and very low p -value (< 0.001). The calculated higher F-value and lower p -value for the photocatalyst dosage (D factor) in comparison with other factors indicated that the photocatalyst dosage is the most important parameter in the system. The results in Table 5 showed that the proposed statistical model is accurately fitted to experimental data. The accuracy of the proposed model should be investigated in detail. Figure 11 shows a linear relationship between experimental data and predicted values in terms of naproxen removal and it confirms the accuracy of the proposed model as all the data accumulated around a 45-degree line. The normal probability plot of the residuals was shown in Fig. 11b and it can be clearly seen a linear scattering of modeling data. The linear scattering means normal distribution of errors in a defined matrix for experimental design. Therefore, the probability of random error intervention and effect of the sequence of experiments is considerably decreased in the proposed model.

Optimization using RSM. An optimization was performed in order to find the optimal operating conditions for the removal of naproxen completely from pharmaceutical synthetic solutions. According to the proposed model, the following independent operating parameters are required for complete removal of naproxen (101.92%): initial naproxen concentration = 18.95 mg/L, initial pH value = 4.55, photocatalyst dosage = 0.49 g/L,

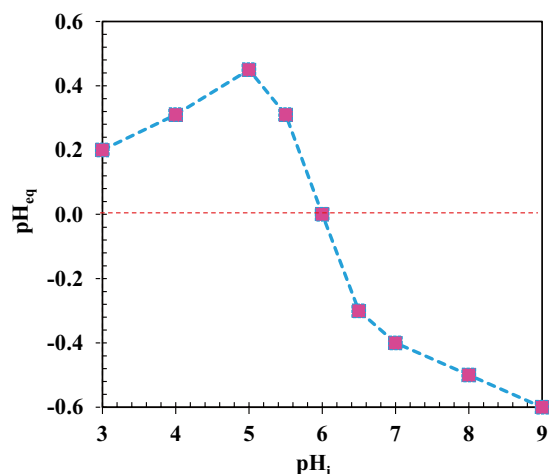


Figure 10. Point of zero charge $\text{ZrO}_2/\text{TiO}_2/\text{Fe}_3\text{O}_4$ photocatalyst.

Source	Sum of Squares	df	Mean Square	F-value	p-value	
Model	5.28	14	0.3770	431.34	<0.0001	Significant
A-NPX Concentration	1.02	1	1.02	1170.41	<0.0001	
B-Time	0.6622	1	0.6622	757.51	<0.0001	
C-pH	0.4464	1	0.4464	510.73	<0.0001	
D-Catalyst Concentration	2.32	1	2.32	2654.05	<0.0001	
AB	0.0027	1	0.0027	3.09	0.0990	
AC	0.1119	1	0.1119	128.00	<0.0001	
AD	0.0355	1	0.0355	40.67	<0.0001	
BC	0.0059	1	0.0059	6.75	0.0202	
BD	0.0013	1	0.0013	1.50	0.2391	
CD	0.0067	1	0.0067	7.61	0.0146	
A ²	0.0500	1	0.0500	57.22	<0.0001	
B ²	0.0353	1	0.0353	40.41	<0.0001	
C ²	0.1073	1	0.1073	122.76	<0.0001	
D ²	0.0672	1	0.0672	76.84	<0.0001	
Residual	0.0131	15	0.0009			
Lack of Fit	0.0088	10	0.0009	1.02	0.5274	Not significant
Pure Error	0.0043	5	0.0009			
Cor Total	5.29	29				

Table 5. ANOVA results for the quadratic model.

time = 74.31 min. Figure 12 illustrates different operating conditions that can be used to achieve complete degradation of naproxen.

Reusability $\text{ZrO}_2/\text{TiO}_2/\text{Fe}_3\text{O}_4$ photocatalyst. The regeneration and re-use of the used or spent photocatalyst is very critical for determining the applicability of the process applied. The used photocatalyst was separated from the synthetic solution using 1.3 Tesla magnetic. Then, it was used for the treatment of pharmaceutical synthetic solution as given in Fig. 13. As can be seen in Fig. 13, the degradation efficiency only display partial reduction after seven cycles for degradation of naproxen, indicating excellent reusability of the synthesized photocatalyst as after 7 runs, its performance for naproxen degradation was decreased only 12%. Additionally, the photocatalyst was placed in distilled water under UV light for 12 h in order to regenerate it. After doing the regeneration process, the photocatalyst was able to degrade the naproxen by about 98.4%. However, after three regenerations, the activity of the photocatalyst decreased by 8.4%. The decrease in performance of photocatalyst may be related to the blocking of active pores due to precipitation of non-sensitive chemicals to light or destroying of effective nanoparticles during the recovery process. Each experiment was replicated three times and an error bar was shown in Fig. 13.

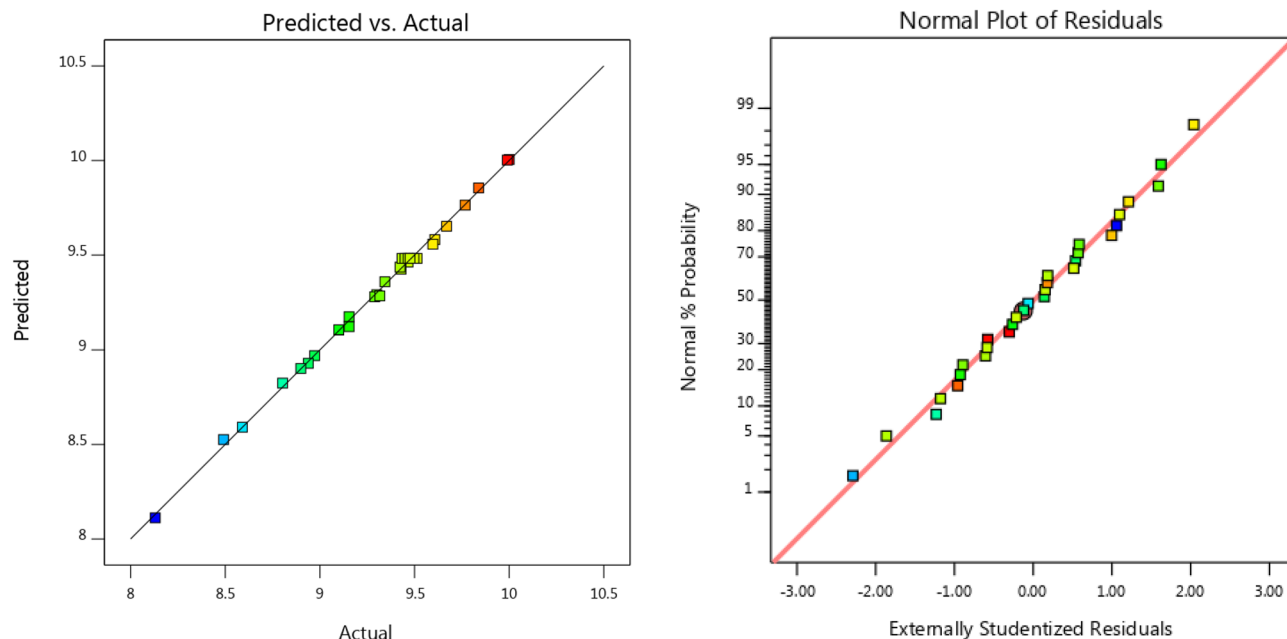


Figure 11. (a) The relationship of predicted and actual values of the RSM model for naproxen removal; (b) the externally studentized residuals versus normal % probability distribution.

Analysis study of naproxen removal kinetics. The removal of naproxen using heterogeneous photocatalyst is divided into two main stages: physical adsorption reaction and chemical reaction. In order to describe the photocatalytic degradation rate of naproxen by plotting $\ln(C_0/C)$ versus time (t), at different concentrations, the Langmuir–Hinshelwood (LH) kinetic model was used¹⁰⁶:

$$\ln \frac{C_i}{C} = k.t \quad (5)$$

where C_i (mg/L), the initial concentration of naproxen and C (mg/L), the concentration at time (t) after irradiation, and k is a pseudo-first-order rate constant. As shown in Fig. 14, the pseudo-first-order rate constant was determined based on a straight-line slope. According to the results of Fig. 14b, the maximum reaction rate at the initial concentration of 5 mg/L naproxen is 0.0514 min^{-1} , which is about 2 times higher than the obtained reaction rate at the initial concentration of 30 mg/L naproxen. The obtained results in Fig. 14b show that reaction rates decrease with increasing concentration. The naproxen adsorbed amount q_e (mg/g) by $\text{ZrO}_2/\text{TiO}_2/\text{Fe}_3\text{O}_4$ nanocomposite was calculated using the following equation (Eq. (6)):

$$q_e = \frac{(C_i - C_e).V}{m} \quad (6)$$

where C_i and C_e are the initial and equilibrium concentrations of naproxen (mg/L), respectively. The volume of naproxen solution (ml) is V and the mass of $\text{ZrO}_2/\text{TiO}_2/\text{Fe}_3\text{O}_4$ nanocomposite (mg) is m . The following equation was used to calculate the percentage of naproxen adsorption (%) (Eq. 7):

$$\text{Adsorption}(\%) = \frac{(C_i - C_e).V}{m} \quad (7)$$

As shown in Fig. 14 when the initial concentration of naproxen was increased from 5 to 30 mg/L, the initial photodegradation rate (r_0) also gradually increased from 0.26 to 0.77 mg/L. It was shown that naproxen photocatalytic degradation occurs on $\text{ZrO}_2/\text{TiO}_2/\text{Fe}_3\text{O}_4$ nanocomposite surfaces and that the rate of photo degradation increases as a function of increasing of adsorption. As the initial concentration of naproxen increases, the coverage of naproxen molecules on the surface of $\text{ZrO}_2/\text{TiO}_2/\text{Fe}_3\text{O}_4$ nanocomposite also increases accordingly. As a result, the electron transfer efficiency of naproxen molecules to the adsorbed surface and the charge produced by the light increases, which leads to an increase in the initial optical decomposition rate (r_0). As a result, the electron transfer efficiency of naproxen molecules, which leads to an increase in the initial photodegradation rate (r_0), increases with increasing adsorbed surface and the produced charge by light. For different initial concentrations, the kinetic constant of naproxen photo degradation gradually decreased (from 0.0514 to 0.0255 min^{-1}), while the R^2 correlation coefficient also decreased from 0.9961 to 0.9817. The relationship between the reaction rate (k) and the initial concentration of the substrate during the photocatalytic process can be generally explained by the following experimental formula (Eq. 8):

$$k = a[\text{NPX}]^n \quad (8)$$

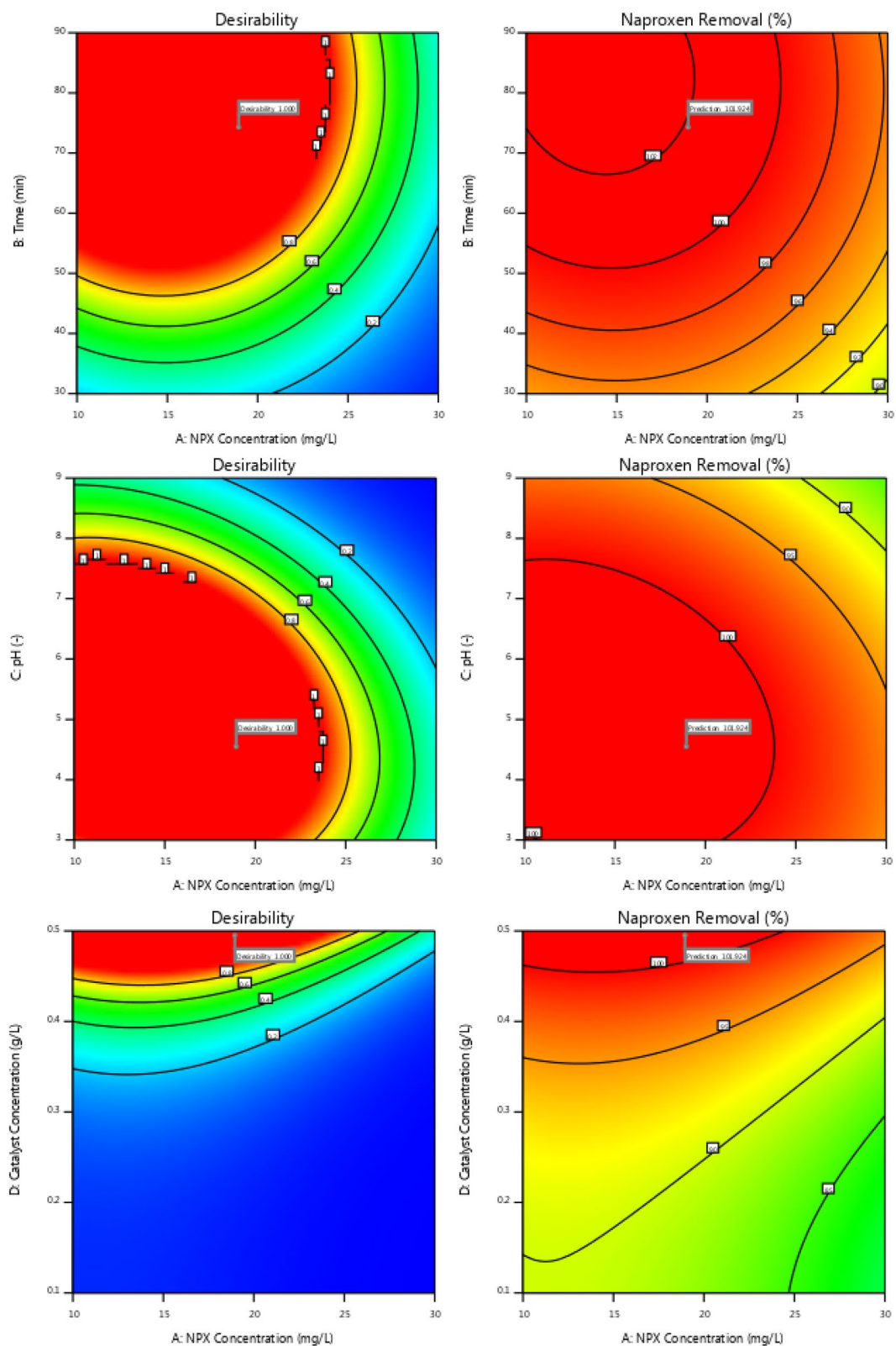


Figure 12. A range of independent variables of pH, photocatalyst dosage, time, and initial naproxen concentration.

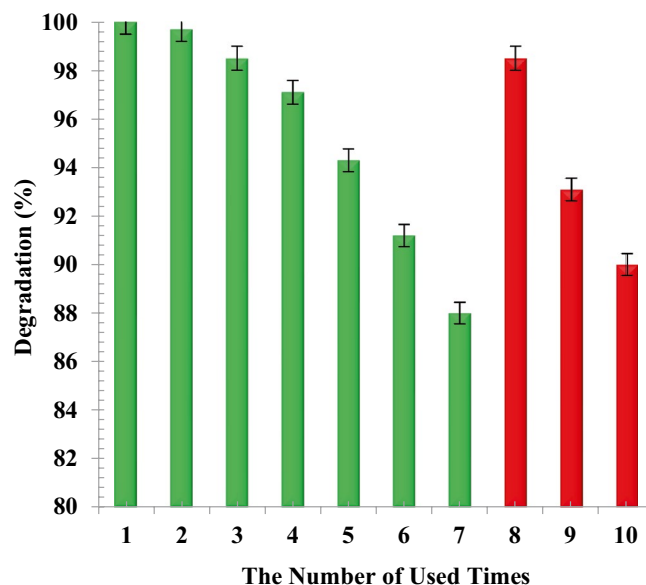


Figure 13. Reusability and regeneration of $\text{ZrO}_2/\text{TiO}_2/\text{Fe}_3\text{O}_4$ photocatalyst for naproxen degradation.

$$\ln k = \ln a + n \ln [\text{NPX}] \quad (9)$$

where n is the correlation index and $[\text{NPX}]$ is the initial concentration (NPX) ($\text{mg}\cdot\text{L}^{-1}$).

Linear regression was used to analyze the relationship between the kinetic constant of NPX photo degradation and its initial concentration (5–30 mg/L). Figure 14 shows that the relationship between reaction rate k and NPX concentration is as follows:

$$\ln k = \ln 0.0196 + 0.2074 \cdot \ln [\text{NPX}] \quad (R^2 = 0.9992) \quad (10)$$

The results showed that the adsorption of naproxen on the surface of $\text{ZrO}_2/\text{TiO}_2/\text{Fe}_3\text{O}_4$ nanoparticles is clearly time-dependent. As shown in Fig. 14a most naproxen removal occurred within the initial 50 min, and after 50 min, naproxen removals occurred almost in the flat part of the graph. The highest percentage of naproxen removal is at the initial concentration of 5 mg/L of solution. In the initial 50 min, two mechanisms were involved in the removal of naproxen: the free active sites at the adsorbent surface, and the generation of hydroxyl ions. Subsequently, a slow rate of naproxen removal was observed.

Different kinetic models were investigated to analyze the kinetic data and determine the kinetic mechanism of naproxen adsorption on the surface of $\text{ZrO}_2/\text{TiO}_2/\text{Fe}_3\text{O}_4$ nanocomposite which is shown in Table 6.

Elovich model shows less linearity in the regression coefficient R^2 ; which was found to be 0.9202, On the other hand, the correlation coefficient value for a Langmuir–Hinshelwood (LH) kinetic model was obtained 0.9992 for NPX and greater than all other adsorption kinetic models. The calculated q_e value was found to be 26.4 mg/g for NPX, which was very close to the obtained experimental values (shown in Table 6). According to the obtained results, it is expected that NPX and its degradation intermediates may be further degraded by reactive species, thus leading to ring openings and eventually oxidation to CO_2 and H_2O . As can be seen in Fig. 15, the possible degradation pathways of NPX are proposed based on the identification of intermediates and mineralization results. The photocatalytic degradation of NPX by $\text{ZrO}_2/\text{TiO}_2/\text{Fe}_3\text{O}_4$ mainly refers to three main pathways including decarboxylation and hydroxylation³⁹. Three possible degradation pathways through oxidation processes are shown in Fig. 15. In the oxidation pathway I, NPX degradation was initiated by the electrophilic additive interaction between the naphthalene ring of NPX and $\cdot\text{OH}$ ^{114–116}. In pathways II and III, NPX oxidation was performed by h^+ and $\cdot\text{O}^{2-}$ and carbon-based radical species were formed by decarboxylation¹¹⁷. All produced intermediates during the process were decomposed by ring-opening reactions to malic acid, succinic acid, propionic acid and acetic acid, and finally mineralized to CO_2 and H_2O ^{39,118,119}.

In order to confirm mineralization, we investigated total organic carbon (TOC) in the degradation of naproxen at ambient temperature and $\text{pH} = 3$. The amount of TOC was decreased with increasing irradiation time (Fig. 16). In this study, the mineralization of naproxen is confirmed using $\text{ZrO}_2/\text{TiO}_2/\text{Fe}_3\text{O}_4$ photocatalysts. TOC removal was obtained 87% after 90 min irradiation. Naproxen may be oxidized to CO_2 , H_2O , and some small molecules, according to TOC results.

As shown in Table 7, in comparison with previous studies, the synthesized photocatalyst in this study had the highest naproxen removal efficiency. The synthesis of ternary nanocomposites confirmed the excellent synergistic effect of these three types of nanoparticles on the photocatalytic process. Based on the Table 7, the synthesized photocatalyst has high specific surface area. In addition, its proper capability in acidic environment increases efficiency and absorption over time for the removal of naproxen at low dosage of catalyst in comparison with other similar synthesized photo catalysts.

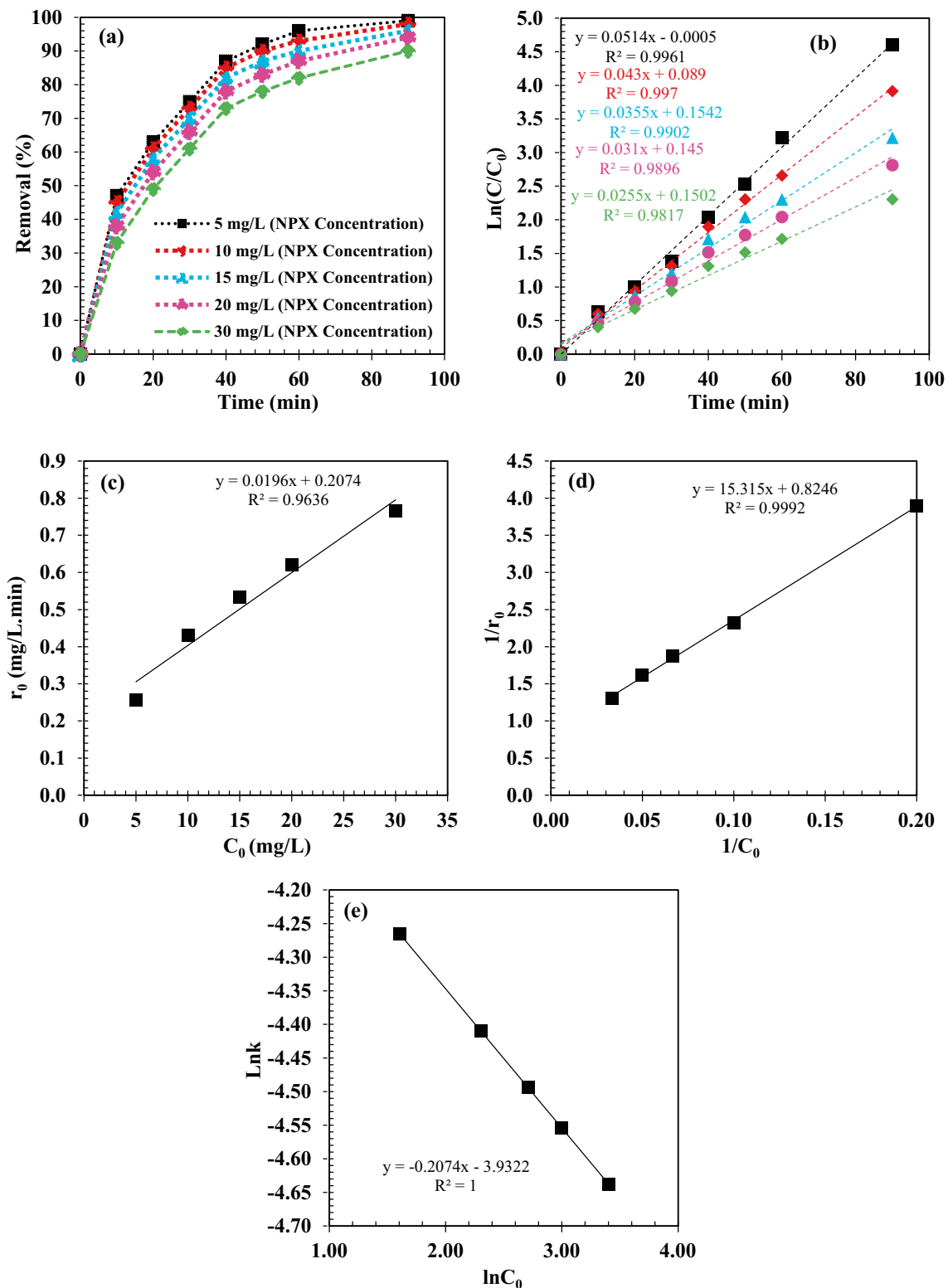


Figure 14. (a) The effect of initial concentrations on NPX removal(%), (b) The effect of initial concentrations of NPX on photo degradation, (c) The initial reaction rate (r_0) as a function of NPX initial concentration (C_0); (d) L-H model of photocatalytic NPX degradation by $ZrO_2/TiO_2/Fe_3O_4$; (e) The effect of different initial concentrations on the NPX photo degradation rate constant.

Model	Equation	Parameter	References
Elovich	$q_t = (1/\beta)(\ln(\alpha\beta)) + (1/\beta)\ln(t)$	R^2	0.9202
		α	67.378
		β	0.313
Weber and Moris	$q_t = C + K_{int}(t)^{1/2}$	R^2	0.9377
		K_{int}	1.984
		C	10.57
Pseudo 2nd order (McKay-Ho)	$(t/q_t) = 1/(K_2 q_e^2) + (1/q_e)t$	R^2	0.9814
		K_2	0.013
		Calculated q_e	26.4
		Experimental q_e	25.7
Pseudo 1st order (Lagergeren)	$\text{Log}(q_e - q_t) = \text{Log } q_e - (K_1/2.303)t$	R^2	0.9891
		K_1	0.085
		Calculated q_e	17.12

Table 6. Equations of adsorption kinetic models for naproxen adsorption on $\text{ZrO}_2/\text{TiO}_2/\text{Fe}_3\text{O}_4$ nanocomposite. q_e : the amount of adsorbed NPX by $\text{ZrO}_2/\text{TiO}_2/\text{Fe}_3\text{O}_4$ nanocomposite (mg/g) [at equilibrium]. q_t : the amount of adsorbed NPX by $\text{ZrO}_2/\text{TiO}_2/\text{Fe}_3\text{O}_4$ nanocomposite (mg/g) [at determined time interval t]. K_1 : rate constant of pseudo 1st order adsorption process (min^{-1}). K_2 : the rate constant of pseudo 2nd order adsorption process ($\text{g mg}^{-1} \text{min}^{-1}$). α : the initial adsorption rate constant (mg/g min). β : constant related to surface coverage and the activation energy for chemisorptions (g/mg). K_{int} : the intraparticle rate constant ($\text{mg/g min}^{1/2}$). C : value about the boundary thickness.

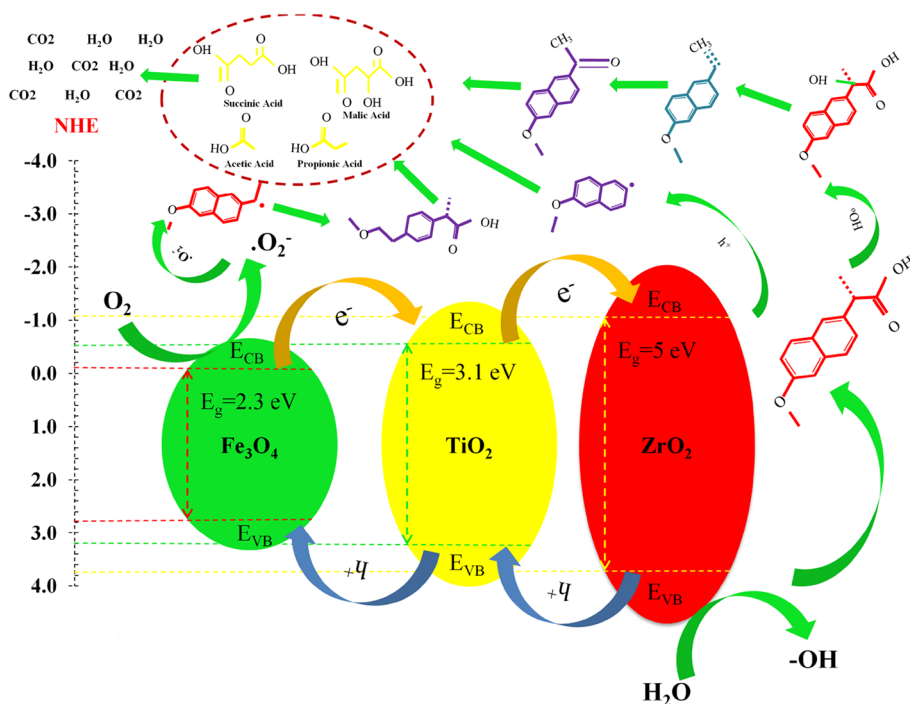


Figure 15. Photo degradation reaction mechanism of NPX by $\text{ZrO}_2/\text{TiO}_2/\text{Fe}_3\text{O}_4$.

Conclusion

In summary, we synthesized a ternary $\text{ZrO}_2/\text{TiO}_2/\text{Fe}_3\text{O}_4$ nanocomposite system using a solid-state dispersion method. Furthermore, its photocatalytic activity towards naproxen degradation was investigated. The effect of operating parameters including initial naproxen concentration, initial pH, photocatalyst dosage, and time on the degradation of naproxen was investigated. Characterization results confirmed the formation of the ternary nanocomposite. The existence of cylindrical and spherical pores in the sample was proved because its N_2 adsorption–desorption hysteresis followed IV-H1 type hysteresis. Based on optimization results using the RSM method, the optimal conditions for the complete removal of naproxen were determined as initial naproxen concentration of 18.95 mg/L, initial pH of 4.55, photocatalyst dosage of 0.49 g/L, and time of 74.31 min. Reusability results showed 12% reduction in naproxen degradation after 7 runs. It was found that Langmuir–Hinshelwood's (LH)

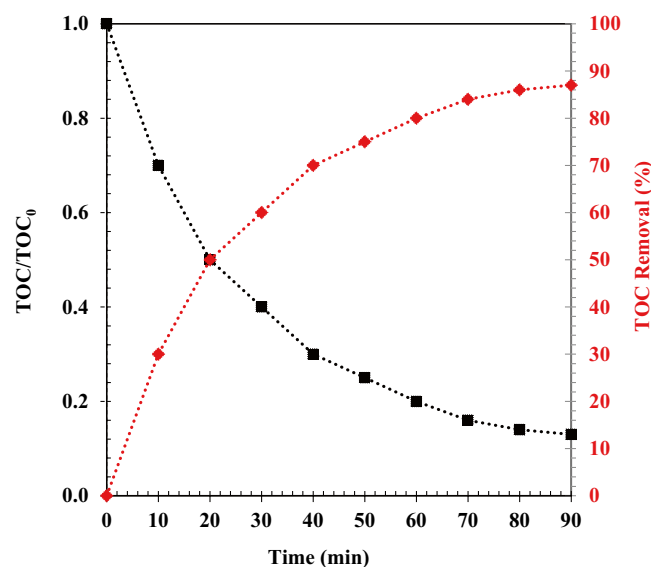


Figure 16. Total organic carbon (TOC) in naproxen wastewater as a function of time and the $\text{ZrO}_2/\text{TiO}_2/\text{Fe}_3\text{O}_4$ photocatalytic activity.

Type of photocatalyst	Surface areas ($\text{m}^2 \text{g}^{-1}$)	NPX concentration (mg/L)	Irradiation time (min)	Catalyst concentration (g/L)	pH	Degradation efficiency (%)	Average pore volume ($\text{cm}^3 \text{g}^{-1}$)	References
$\text{ZrO}_2/\text{TiO}_2/\text{Fe}_3\text{O}_4$	280	10	90	0.5	3	100	0.92	Present work
TiO_2	55	0.184	120	0.1	6.15	40	–	120
$\text{MoS}_2\text{-CeO}_2\text{-ZrO}_2$	39.45	11.51	40	0.5	5.8	21	–	121
$\text{P}_{25}\text{-TiO}_2/\text{TEOS}$	–	5	600	0.003	6	94	–	122
HTNM	53.67	0.5	180	1.5	7	99.9	0.32	39
ZnO	–	40	120	0.5	7	98.7	–	123
$\text{Fe}_3\text{O}_4/\text{MWCNTs}$	144	10	–	0.4	7	83	0.24	124
N-doped $\text{TiO}_2/\text{SiO}_2/\text{Fe}_3\text{O}_4$	232.41	9.33	217.08	0.06	4.29	96.32	–	125

Table 7. Comparison of naproxen removal efficiency in the presence of synthesized photocatalyst under optimum process conditions.

kinetic model was linear. The regression coefficient (R^2) was obtained 0.9992 and it was greater than all other adsorption kinetic models.

Received: 6 August 2021; Accepted: 10 June 2022

Published online: 20 June 2022

References

- Lumbaqué, E. C. *et al.* Degradation of pharmaceuticals in wastewater matrices through solar light-driven photocatalyst prepared from petrochemical waste. *Environ. Sci. Pollut. Res.* **28**(19), 24124–24137 (2021).
- Gao, J. *et al.* Using prescription and wastewater data to estimate the correction factors of atenolol, carbamazepine, and naproxen for wastewater-based epidemiology applications. *Environ. Sci. Technol.* **55**(11), 7551–7560 (2021).
- Petrovic, M., Radjenovic, J. & Barcelo, D. Advanced oxidation processes (AOPs) applied for wastewater and drinking water treatment. Elimination of pharmaceuticals. *Holist. Approach Environ.* **1**(2), 63–74 (2011).
- Liu, Z.-H., Kanjo, Y. & Mizutani, S. Removal mechanisms for endocrine disrupting compounds (EDCs) in wastewater treatment—Physical means, biodegradation, and chemical advanced oxidation: A review. *Sci. Total Environ.* **407**(2), 731–748 (2009).
- Wang, J. & Wang, S. Removal of pharmaceuticals and personal care products (PPCPs) from wastewater: A review. *J. Environ. Manage.* **182**, 620–640 (2016).
- Mojiri, A. *et al.* Removal performance and optimisation of pharmaceutical micropollutants from synthetic domestic wastewater by hybrid treatment. *J. Contam. Hydrol.* **235**, 103736 (2020).
- Khan, A. H. *et al.* Application of advanced oxidation processes followed by different treatment technologies for hospital wastewater treatment. *J. Clean. Prod.* **269**, 122411 (2020).
- Kilic, M. Y. *et al.* Photochemical treatment of tyrosol, a model phenolic compound present in olive mill wastewater, by hydroxyl and sulfate radical-based advanced oxidation processes (AOPs). *J. Hazard. Mater.* **367**, 734–742 (2019).
- Bin, A. K. & Sobera-Madej, S. Comparison of the advanced oxidation processes (UV, UV/ H_2O_2 and O_3) for the removal of antibiotic substances during wastewater treatment. *Ozone Sci. Eng.* **34**(2), 136–139 (2012).

10. Zhang, Q. *et al.* Efficient degradation of typical pharmaceuticals in water using a novel TiO₂/ONLH nano-photocatalyst under natural sunlight. *J. Hazard. Mater.* **403**, 123582 (2021).
11. Li, C. *et al.* Degradation characteristics of four major pollutants in chemical pharmaceutical wastewater by Fenton process. *J. Environ. Chem. Eng.* **9**(1), 104564 (2021).
12. Feng, L. *et al.* Removal of residual anti-inflammatory and analgesic pharmaceuticals from aqueous systems by electrochemical advanced oxidation processes. A review. *Chem. Eng. J.* **228**, 944–964 (2013).
13. Peng, G. *et al.* Adsorption and catalytic oxidation of pharmaceuticals by nitrogen-doped reduced graphene oxide/Fe₃O₄ nanocomposite. *Chem. Eng. J.* **341**, 361–370 (2018).
14. Adityosulindro, S. *et al.* Sonolysis and sono-Fenton oxidation for removal of ibuprofen in (waste) water. *Ultrason. Sonochem.* **39**, 889–896 (2017).
15. Deng, Y. & Zhao, R. Advanced oxidation processes (AOPs) in wastewater treatment. *Curr. Pollut. Rep.* **1**(3), 167–176 (2015).
16. Giannakoudakis, D. A. *et al.* Boosting the photoactivity of grafted titania: Ultrasound-driven synthesis of a multi-phase heterogeneous nano-architected photocatalyst. *Adv. Func. Mater.* **31**(1), 2007115 (2021).
17. Chen, W. *et al.* Direct Z-scheme 2D/2D MnIn₂S₄/g-C₃N₄ architectures with highly efficient photocatalytic activities towards treatment of pharmaceutical wastewater and hydrogen evolution. *Chem. Eng. J.* **359**, 244–253 (2019).
18. Vaiano, V. *et al.* Photocatalytic removal of spiramycin from wastewater under visible light with N-doped TiO₂ photocatalysts. *Chem. Eng. J.* **261**, 3–8 (2015).
19. Elmolla, E. S. & Chaudhuri, M. The feasibility of using combined TiO₂ photocatalysis-SBR process for antibiotic wastewater treatment. *Desalination* **272**(1), 218–224 (2011).
20. Han, F. *et al.* Tailored titanium dioxide photocatalysts for the degradation of organic dyes in wastewater treatment: A review. *Appl. Catal. A* **359**(1), 25–40 (2009).
21. Da Dalt, S., Alves, A. K. & Bergmann, C. P. Photocatalytic degradation of methyl orange dye in water solutions in the presence of MWCNT/TiO₂ composites. *Mater. Res. Bull.* **48**(5), 1845–1850 (2013).
22. Luttrell, T. *et al.* Why is anatase a better photocatalyst than rutile?—Model studies on epitaxial TiO₂ films. *Sci. Rep.* **4**, 1–8 (2014).
23. Matos, J. *et al.* Influence of anatase and rutile phase in TiO₂ upon the photocatalytic degradation of methylene blue under solar irradiation in presence of activated carbon. *Water Sci. Technol.: J. Int. Assoc. Water Pollut. Res.* **69**(11), 2184–2190 (2014).
24. Xu, N. *et al.* Effects of particle size of TiO₂ on photocatalytic degradation of methylene blue in aqueous suspensions. *Ind. Eng. Chem. Res.* **38**, 373–379 (1999).
25. Shan, A. Y., Ghazi, T. I. M. & Rashid, S. A. Immobilisation of titanium dioxide onto supporting materials in heterogeneous photocatalysis: A review. *Appl. Catal. A* **389**(1), 1–8 (2010).
26. Xu, Z. *et al.* Structure, luminescence properties and photocatalytic activity of europium doped-TiO₂ nanoparticles. *J. Mater. Sci.* **40**(6), 1539–1541 (2005).
27. McManamon, C., Holmes, J. D. & Morris, M. A. Improved photocatalytic degradation rates of phenol achieved using novel porous ZrO₂-doped TiO₂ nanoparticulate powders. *J. Hazard. Mater.* **193**, 120–127 (2011).
28. Sandoval, S. *et al.* Europium-doped TiO₂ hollow nanoshells: Two-photon imaging of cell binding. *Chem. Mater.* **24**(21), 4222–4230 (2012).
29. Wang, X. *et al.* ZrO₂-modified mesoporous nanocrystalline TiO₂-xN_x as efficient visible light photocatalysts. *Environ. Sci. Technol.* **40**(7), 2369–2374 (2006).
30. Jung, K. Y. & Park, S. B. Photoactivity of SiO₂/TiO₂ and ZrO₂/TiO₂ mixed oxides prepared by sol-gel method. *Mater. Lett.* **58**(22), 2897–2900 (2004).
31. Fu, X. *et al.* Enhanced photocatalytic performance of titania-based binary metal oxides: TiO₂/SiO₂ and TiO₂/ZrO₂. *Environ. Sci. Technol.* **30**(2), 647–653 (1996).
32. Rao, Y. *et al.* Photocatalytic activity of G-TiO₂@Fe₃O₄ with persulfate for degradation of alizarin red S under visible light. *Chemosphere* **266**, 129236 (2021).
33. Izadpanah, M. *et al.* Aquatic center sewage reclamation and water reuse, using an integrated system combining adsorption, RO membrane system, and TiO₂/Fe₃O₄ photocatalytic oxidation. *J. Environ. Chem. Eng.* **9**(1), 104957 (2021).
34. Chu, A.-C. *et al.* Magnetic Fe₃O₄@TiO₂ nanocomposites to degrade bisphenol A, one emerging contaminant, under visible and long wavelength UV light irradiation. *J. Environ. Chem. Eng.* **9**(4), 105539 (2021).
35. Narzary, S. *et al.* Visible light active, magnetically retrievable Fe₃O₄@SiO₂@g-C₃N₄/TiO₂ nanocomposite as efficient photocatalyst for removal of dye pollutants. *J. Environ. Chem. Eng.* **8**(5), 104373 (2020).
36. Zhao, D. *et al.* Use of nonsteroidal anti-inflammatory drugs for COVID-19 infection: Adjunct therapy?. *Cardiol. Rev.* **28**(6), 303–307 (2020).
37. Yousefifard, M. *et al.* Non-steroidal anti-inflammatory drugs in management of COVID-19; A systematic review on current evidence. *Int. J. Clin. Pract.* **74**(9), e13557 (2020).
38. Fan, G. *et al.* Visible-light-driven photocatalytic degradation of naproxen by Bi-modified titanate nanobulks: Synthesis, degradation pathway and mechanism. *J. Photochem. Photobiol. A* **386**, 112108 (2020).
39. Fan, G. *et al.* Photocatalytic degradation of naproxen by a H₂O₂-modified titanate nanomaterial under visible light irradiation. *Catal. Sci. Technol.* **9**(17), 4614–4628 (2019).
40. Gutierrez, A. M., Dziubla, T. D. & Hilt, J. Z. Recent advances on iron oxide magnetic nanoparticles as sorbents of organic pollutants in water and wastewater treatment. *Rev. Environ. Health* **32**(1–2), 111–117 (2017).
41. Marjani, A. *et al.* Synthesis of alginate-coated magnetic nanocatalyst containing high-performance integrated enzyme for phenol removal. *J. Environ. Chem. Eng.* **9**(1), 104884 (2021).
42. Sarkar, S., Chakraborty, S. & Bhattacharjee, C. Photocatalytic degradation of pharmaceutical wastes by alginate supported TiO₂ nanoparticles in packed bed photo reactor (PBPR). *Ecotoxicol. Environ. Saf.* **121**, 263–270 (2015).
43. Ghenaatgar, A., Tehrani, R. M. & Khadir, A. Photocatalytic degradation and mineralization of dexamethasone using WO₃ and ZrO₂ nanoparticles: Optimization of operational parameters and kinetic studies. *J. Water Process Eng.* **32**, 100969 (2019).
44. Radu, T. *et al.* Evaluation of physico-chemical properties and biocompatibility of new surface functionalized Fe₃O₄ clusters of nanoparticles. *Appl. Surf. Sci.* **501**, 144267 (2020).
45. Das, D. *et al.* Preparation, physico-chemical characterization and catalytic activity of sulphated ZrO₂-TiO₂ mixed oxides. *J. Mol. Catal. A: Chem.* **189**(2), 271–282 (2002).
46. Chen, X. & Mao, S. S. Titanium dioxide nanomaterials: Synthesis, properties, modifications, and applications. *Chem. Rev.* **107**(7), 2891–2959 (2007).
47. Reyes-Coronado, D. *et al.* Phase-pure TiO₂ nanoparticles: Anatase, brookite and rutile. *Nanotechnology* **19**(14), 145605 (2008).
48. Navio, J. & Colón, G. Heterogeneous photocatalytic oxidation of liquid isopropanol by TiO₂, ZrO₂ and ZrTiO₄ powders. *Stud. Surf. Sci. Catal.* **82**, 721–728 (1994).
49. Wiemhöfer, H. D. & Vohrer, U. Spectroscopy and thermodynamics of electrons in yttria-stabilized zirconia. *Ber. Bunsenges. Phys. Chem.* **96**(11), 1646–1652 (1992).
50. Preusser, S., Stimming, U. & Wippermann, K. An optical and electrochemical investigation of ZrO₂ thin films (from nm to mm thickness). *Electrochim. Acta* **39**(8–9), 1273–1280 (1994).
51. Bendoraitis, J. & Salomon, R. Optical energy gaps in the monoclinic oxides of hafnium and zirconium and their solid solutions¹. *J. Phys. Chem.* **69**(10), 3666–3667 (1965).

52. Newmark, A. & Stimming, U. Photoelectrochemical studies of passive films on zirconium and amorphous iron–zirconium alloys. *Langmuir* **3**(6), 905–910 (1987).
53. Sato, S. & Kadowaki, T. Photocatalytic activities of metal oxide semiconductors for oxygen isotope exchange and oxidation reactions. *J. Catal.* **106**(1), 295–300 (1987).
54. Botta, S. G. *et al.* Photocatalytic properties of ZrO₂ and Fe/ZrO₂ semiconductors prepared by a sol–gel technique. *J. Photochem. Photobiol. A* **129**(1–2), 89–99 (1999).
55. Sayama, K. & Arakawa, H. Photocatalytic decomposition of water and photocatalytic reduction of carbon dioxide over zirconia catalyst. *J. Phys. Chem.* **97**(3), 531–533 (1993).
56. Sayama, K. & Arakawa, H. Effect of carbonate addition on the photocatalytic decomposition of liquid water over a ZrO₂ catalyst. *J. Photochem. Photobiol. A* **94**(1), 67–76 (1996).
57. Aydar, A. Y. Utilization of Response Surface Methodology in Optimization of Extraction of Plant Materials. In *Statistical Approaches with Emphasis on Design of Experiments Applied to Chemical Processes* (ed. Silva, V.) 157–169 (BoD, 2018).
58. Khuri, A. I. & Mukhopadhyay, S. Response surface methodology. *Wiley Interdiscip. Rev.: Comput. Stat.* **2**(2), 128–149 (2010).
59. Diaz-Urribe, C. *et al.* Photocatalytic activity of Ag–TiO₂ composites deposited by photoreduction under UV irradiation. *Int. J. Photoenergy* **2018**, 1–8 (2018).
60. Kambur, A., Pozan, G. S. & Boz, I. Preparation, characterization and photocatalytic activity of TiO₂–ZrO₂ binary oxide nanoparticles. *Appl. Catal. B* **115**, 149–158 (2012).
61. Poliseti, S., Deshpande, P. A. & Madras, G. Photocatalytic activity of combustion synthesized ZrO₂ and ZrO₂–TiO₂ mixed oxides. *Ind. Eng. Chem. Res.* **50**(23), 12915–12924 (2011).
62. Davar, F., Majedi, A. & Abbasi, A. Synthesis of Fe₃O₄@ZrO₂ core–shell nanoparticles through new approach and its solar light photocatalyst application. *J. Mater. Sci.: Mater. Electron.* **28**(6), 4871–4878 (2017).
63. Shojaei, A. F., Shams-Nateri, A. & Ghomashpasand, M. Comparative study of photocatalytic activities of magnetically separable WO₃/TiO₂/Fe₃O₄ nanocomposites and TiO₂, WO₃/TiO₂ and TiO₂/Fe₃O₄ under visible light irradiation. *Superlattices Microstruct.* **88**, 211–224 (2015).
64. Fallah Shojaei, A., Shams-Nateri, A. & Ghomashpasand, M. Magnetically recyclable Fe³⁺/TiO₂@Fe₃O₄ nanocomposites towards degradation of direct blue 71 under visible-light irradiation. *Micro Nano Lett.* **12**(3), 161–165 (2017).
65. El Ghandoor, H. *et al.* Synthesis and some physical properties of magnetite (Fe₃O₄) nanoparticles. *Int. J. Electrochem. Sci* **7**(6), 5734–5745 (2012).
66. Taghizadeh, M. T. & Vatanparast, M. Ultrasonic-assisted synthesis of ZrO₂ nanoparticles and their application to improve the chemical stability of Nafion membrane in proton exchange membrane (PEM) fuel cells. *J. Colloid Interface Sci.* **483**, 1–10 (2016).
67. Reddy, C. V. *et al.* Synthesis and characterization of pure tetragonal ZrO₂ nanoparticles with enhanced photocatalytic activity. *Ceram. Int.* **44**(6), 6940–6948 (2018).
68. Aslan, N. & Cebeci, Y. Application of Box–Behnken design and response surface methodology for modeling of some Turkish coals. *Fuel* **86**(1–2), 90–97 (2007).
69. Berkani, M. *et al.* Combination of a Box–Behnken design technique with response surface methodology for optimization of the photocatalytic mineralization of CI Basic Red 46 dye from aqueous solution. *Arab. J. Chem.* **13**(11), 8338–8346 (2020).
70. Chintaparty, C. R. Influence of calcination temperature on structural, optical, dielectric properties of nano zirconium oxide. *Optik* **127**(11), 4889–4893 (2016).
71. Mushtaq, K. *et al.* Synthesis and characterization of TiO₂ via sol–gel method for efficient photocatalytic degradation of antibiotic ofloxacin. *Inorg. Nano-Metal Chem.* **50**(7), 580–586 (2020).
72. He, Q. *et al.* A novel biomaterial—Fe₃O₄:TiO₂ core–shell nano particle with magnetic performance and high visible light photocatalytic activity. *Opt. Mater.* **31**(2), 380–384 (2008).
73. Mullet, M. *et al.* A simple and accurate determination of the point of zero charge of ceramic membranes. *Desalination* **121**(1), 41–48 (1999).
74. Heshmatpour, F. & Aghakhanpour, R. B. Synthesis and characterization of nanocrystalline zirconia powder by simple sol–gel method with glucose and fructose as organic additives. *Powder Technol.* **205**(1), 193–200 (2011).
75. Zhang, W. *et al.* Raman scattering study on anatase TiO₂ nanocrystals. *J. Phys. D Appl. Phys.* **33**(8), 912 (2000).
76. Mahshid, S. *et al.* Mixed-phase TiO₂ nanoparticles preparation using sol–gel method. *J. Alloy. Compd.* **478**(1–2), 586–589 (2009).
77. Theivasanthi, T. & M. Alagar, *Titanium dioxide (TiO2) nanoparticles XRD analyses: An insight.* arXiv preprint [arXiv:1307.1091](https://arxiv.org/abs/1307.1091) (2013).
78. Sridevi, A. *et al.* A facile synthesis of TiO₂/BiOCl and TiO₂/BiOCl/La₂O₃ heterostructure photocatalyst for enhanced charge separation efficiency with improved UV-light catalytic activity towards Rhodamine B and Reactive Yellow 86. *Inorg. Chem. Commun.* **130**, 108715 (2021).
79. Zhuang, L. *et al.* Preparation and characterization of Fe₃O₄ particles with novel nanosheets morphology and magnetochromatic property by a modified solvothermal method. *Sci. Rep.* **5**(1), 9320 (2015).
80. Klug, H. P. & Alexander, L. E. *X-Ray Diffraction Procedures: For Polycrystalline and Amorphous Materials* (Wiley, 1974).
81. Patra, J. K. & Baek, K.-H. Green nanobiotechnology: Factors affecting synthesis and characterization techniques. *J. Nanomater.* **2014**, 417305 (2014).
82. Laha, S. C. *et al.* Cerium containing MCM-41-type mesoporous materials and their acidic and redox catalytic properties. *J. Catal.* **207**(2), 213–223 (2002).
83. Rahmani Vahid, B. & Haghghi, M. Biodiesel production from sunflower oil over MgO/MgAl₂O₄ nanocatalyst: Effect of fuel type on catalyst nanostructure and performance. *Energy Convers. Manage.* **134**, 290–300 (2017).
84. Nayebedeh, H. *et al.* Fabrication of carbonated alumina doped by calcium oxide via microwave combustion method used as nanocatalyst in biodiesel production: Influence of carbon source type. *Energy Convers. Manage.* **171**, 566–575 (2018).
85. Vivekanandhan, S. *et al.* Acrylamide assisted polymeric citrate route for the synthesis of nanocrystalline ZrO₂ powder. *Mater. Chem. Phys.* **120**(1), 148–154 (2010).
86. Abazari, R., Mahjoub, A. R. & Sanati, S. A facile and efficient preparation of anatase titania nanoparticles in micelle nanoreactors: Morphology, structure, and their high photocatalytic activity under UV light illumination. *RSC Adv.* **4**(99), 56406–56414 (2014).
87. Antić, Ž *et al.* Multisite luminescence of rare earth doped TiO₂ anatase nanoparticles. *Mater. Chem. Phys.* **135**(2), 1064–1069 (2012).
88. Gangopadhyay, P. *et al.* Magnetite-polymethylmethacrylate core–shell nanocomposites: Applications in all-optical magnetometers. *Nonlinear Opt. Quantum Opt.: Concepts Mod. Opt.* **41**(1), 87–104 (2010).
89. Hariharan, D. *et al.* Visible light active photocatalyst: Hydrothermal green synthesized TiO₂ NPs for degradation of picric acid. *Mater. Lett.* **222**, 45–49 (2018).
90. Su, C. *et al.* Fabrication of Ag/TiO₂ nanoheterostructures with visible light photocatalytic function via a solvothermal approach. *CrystEngComm* **14**(11), 3989–3999 (2012).
91. Rivera, V. *et al.* Near-infrared light emission of Er³⁺-doped zirconium oxide thin films: An optical, structural and XPS study. *J. Alloy. Compd.* **619**, 800–806 (2015).
92. Xu, X. *et al.* Size dependence of defect-induced room temperature ferromagnetism in undoped ZnO nanoparticles. *J. Phys. Chem. C* **116**(15), 8813–8818 (2012).

93. Zheng, W. *et al.* Interpenetrated networks between graphitic carbon infilling and ultrafine TiO₂ Nanocrystals with patterned macroporous structure for high-performance lithium ion batteries. *ACS Appl. Mater. Interfaces*. **9**(24), 20491–20500 (2017).
94. Chary, K. V. R. *et al.* Characterization and reactivity of copper oxide catalysts supported on TiO₂-ZrO₂. *J. Phys. Chem. B* **109**(19), 9437–9444 (2005).
95. Li, M. *et al.* Hierarchically macro-mesoporous ZrO₂-TiO₂ composites with enhanced photocatalytic activity. *Ceram. Int.* **41**(4), 5749–5757 (2015).
96. Zhao, J. *et al.* Solvothermal synthesis, characterization and photocatalytic property of zirconium dioxide doped titanium dioxide spinous hollow microspheres with sunflower pollen as bio-templates. *J. Colloid Interface Sci.* **529**, 111–121 (2018).
97. Ran, F.-Y. *et al.* Angle-resolved photoemission study of Fe₃O₄ (0 0 1) films across Verwey transition. *J. Phys. D Appl. Phys.* **45**(27), 275002 (2012).
98. Lai, L.-J. & Su, C.-S. Luminescence excitation and near edge X-ray absorption spectra of Er₂O₃ dopant on zirconia ceramics. *Mater. Chem. Phys.* **62**(2), 148–152 (2000).
99. Luo, S. *et al.* Synthesis and low-temperature photoluminescence properties of SnO₂ nanowires and nanobelts. *Nanotechnology* **17**(6), 1695 (2006).
100. He, J. H. *et al.* Beaklike SnO₂ nanorods with strong photoluminescent and field-emission properties. *Small* **2**(1), 116–120 (2006).
101. Liqiang, J. *et al.* Review of photoluminescence performance of nano-sized semiconductor materials and its relationships with photocatalytic activity. *Sol. Energy Mater. Sol. Cells* **90**(12), 1773–1787 (2006).
102. Liqiang, J. *et al.* The preparation and characterization of La doped TiO₂ nanoparticles and their photocatalytic activity. *J. Solid State Chem.* **177**(10), 3375–3382 (2004).
103. Ramakrishna, G. *et al.* Dynamics of interfacial electron transfer from photoexcited quinzarin (Qz) into the conduction band of TiO₂ and surface states of ZrO₂ nanoparticles. *J. Phys. Chem. B* **108**(15), 4775–4783 (2004).
104. Wu, J.-C. *et al.* Nonoxidative dehydrogenation of ethylbenzene over TiO₂-ZrO₂ catalysts: II. The effect of pretreatment on surface properties and catalytic activities. *J. Catal.* **87**(1), 98–107 (1984).
105. Kumari, L. *et al.* Controlled hydrothermal synthesis of zirconium oxide nanostructures and their optical properties. *Cryst. Growth Des.* **9**(9), 3874–3880 (2009).
106. Kumar, K. V., Porkodi, K. & Rocha, F. Langmuir–Hinshelwood kinetics—A theoretical study. *Catal. Commun.* **9**(1), 82–84 (2008).
107. Dada, A. *et al.* Langmuir, Freundlich, Temkin and Dubinin–Radushkevich isotherms studies of equilibrium sorption of Zn²⁺ onto phosphoric acid modified rice husk. *IOSR J. Appl. Chem.* **3**(1), 38–45 (2012).
108. Ahmed, M. J. Adsorption of non-steroidal anti-inflammatory drugs from aqueous solution using activated carbons. *J. Environ. Manage.* **190**, 274–282 (2017).
109. Husein, D. Z. Adsorption and removal of mercury ions from aqueous solution using raw and chemically modified Egyptian mandarin peel. *Desalin. Water Treat.* **51**(34–36), 6761–6769 (2013).
110. Kavitha, D. & Namasivayam, C. Experimental and kinetic studies on methylene blue adsorption by coir pith carbon. *Biores. Technol.* **98**(1), 14–21 (2007).
111. Erhayem, M. *et al.* Isotherm, kinetic and thermodynamic studies for the sorption of mercury (II) onto activated carbon from *Rosmarinus officinalis* leaves. *Am. J. Anal. Chem.* **6**(01), 1 (2015).
112. Ho, Y.-S. & McKay, G. Pseudo-second order model for sorption processes. *Process Biochem.* **34**(5), 451–465 (1999).
113. Lagergren, S. K. About the theory of so-called adsorption of soluble substances. *Sven. Vetenskapsakad. Handlingar* **24**, 1–39 (1898).
114. Arany, E. *et al.* Degradation of naproxen by UV, VUV photolysis and their combination. *J. Hazard. Mater.* **262**, 151–157 (2013).
115. Dulova, N., Kattel, E. & Trapido, M. Degradation of naproxen by ferrous ion-activated hydrogen peroxide, persulfate and combined hydrogen peroxide/persulfate processes: The effect of citric acid addition. *Chem. Eng. J.* **318**, 254–263 (2017).
116. Chi, H. *et al.* Hydroxylamine enhanced degradation of naproxen in Cu²⁺ activated peroxymonosulfate system at acidic condition: Efficiency, mechanisms and pathway. *Chem. Eng. J.* **361**, 764–772 (2019).
117. Wang, F. *et al.* Novel ternary photocatalyst of single atom-dispersed silver and carbon quantum dots co-loaded with ultrathin g-C₃N₄ for broad spectrum photocatalytic degradation of naproxen. *Appl. Catal. B* **221**, 510–520 (2018).
118. Gao, Y.-Q. *et al.* Kinetics and mechanistic investigation into the degradation of naproxen by a UV/chlorine process. *RSC Adv.* **7**(53), 33627–33634 (2017).
119. Jallouli, N. *et al.* UV and solar photo-degradation of naproxen: TiO₂ catalyst effect, reaction kinetics, products identification and toxicity assessment. *J. Hazard. Mater.* **304**, 329–336 (2016).
120. Méndez-Arriaga, F., Gimenez, J. & Esplugas, S. Photolysis and TiO₂ photocatalytic treatment of naproxen: Degradation, mineralization, intermediates and toxicity. *J. Adv. Oxid. Technol.* **11**(3), 435–444 (2008).
121. Talukdar, K. *et al.* Rational construction of CeO₂-ZrO₂@MoS₂ hybrid nanoflowers for enhanced sonophotocatalytic degradation of naproxen: Mechanisms and degradation pathways. *Compos. B Eng.* **215**, 108780 (2021).
122. Zhang, H. *et al.* Photocatalytic degradation of four non-steroidal anti-inflammatory drugs in water under visible light by P25-TiO₂/tetraethyl orthosilicate film and determination via ultra performance liquid chromatography electrospray tandem mass spectrometry. *Chem. Eng. J.* **262**, 1108–1115 (2015).
123. Sabouni, R. & Gomaa, H. Photocatalytic degradation of pharmaceutical micro-pollutants using ZnO. *Environ. Sci. Pollut. Res. Int.* **26**(6), 5372–5380 (2019).
124. Huacalco-Aguilar, Y. *et al.* Naproxen removal by CWPO with Fe₃O₄/multi-walled carbon nanotubes in a fixed-bed reactor. *J. Environ. Chem. Eng.* **9**(2), 105110 (2021).
125. Amini, Z. *et al.* Synthesis of N-doped TiO₂/SiO₂/Fe₃O₄ magnetic nanocomposites as a novel purple LED illumination-driven photocatalyst for photocatalytic and photoelectrocatalytic degradation of naproxen: Optimization and different scavenger agents study. *J. Environ. Sci. Health Part A* **54**(12), 1254–1267 (2019).

Author contributions

M.H.Z.: conceptualization, methodology, experimental, resources, reviewing and editing, original draft preparation. A.M.-Z.: conceptualization, methodology, experimental, resources, supervision, reviewing and editing.

Competing interests

The authors declare no competing interests.

Additional information

Correspondence and requests for materials should be addressed to M.H.Z.

Reprints and permissions information is available at www.nature.com/reprints.

Publisher's note Springer Nature remains neutral with regard to jurisdictional claims in published maps and institutional affiliations.



Open Access This article is licensed under a Creative Commons Attribution 4.0 International License, which permits use, sharing, adaptation, distribution and reproduction in any medium or format, as long as you give appropriate credit to the original author(s) and the source, provide a link to the Creative Commons licence, and indicate if changes were made. The images or other third party material in this article are included in the article's Creative Commons licence, unless indicated otherwise in a credit line to the material. If material is not included in the article's Creative Commons licence and your intended use is not permitted by statutory regulation or exceeds the permitted use, you will need to obtain permission directly from the copyright holder. To view a copy of this licence, visit <http://creativecommons.org/licenses/by/4.0/>.

© The Author(s) 2022